Politecnico di Torino

DIPARTIMENTO DI INGEGNERIA MECCANICA E AEROSPAZIALE
Corso di Laurea Magistrale in Mechanical engineering

Tesi di laurea magistrale

Chemical, microstructural and nanoindentation characterization of Ni-Fe alloys: experimental and numerical methods

Relatore:
Prof. Giovanni Maizza

Candidato:
Silvia Pomes

Anno Accademico 2018/2019

"Finding a problem
is finding a way"

Abstract

Research in nanocrystalline materials is growing due to their peculiar mechanical and functional properties. In this thesis, four samples of DC electrodeposited Ni-Fe alloys are considered, with different thickness and heat treatment history. A numerical simulation of nanoindentation test with Berkovich indenter has been implemented.

Nanoindentation tests have been performed, both on top and cross section surfaces of the specimen, to investigate room temperature creep and understand the influence of sample thickness, peak load and hold time on such behaviour. Chemical and microstructural analysis, namely EDS, EBSD and EELS alongside SEM and TEM observation, have been carried out on as deposited and annealed samples, both with and without indentation mark, to gain knowledge on composition, orientation and possible deformation mechanisms in nanocrystalline Ni-Fe.

Numerical simulation has been developed as a 3D model and specific geometries have been introduced in order to partialize the problem and save on computation cost.

Contents

List of Figures

List of Tables

1 Introduction

"When we get to the very, very small world, we have a lot of new things that would happen that represent completely new opportunities for design."

Avant-garde ideas about the "very, very small world" were shared by Richard Feynman,in 1960, in his lecture "There's plenty of room at the bottom" [20] and in 1974, at Tokyo University of Science, the word nano-technology was coined by Norio Taniguchi, who went on to pioneer the application of energy beam techniques to ultra precision materials processing [48]. Nanomaterials became reality and were denoted as materials in which at least one characteristic dimension is between 1 and $100nm$ ($1nm = 10^{-9}m$).

A class of interest of nanomaterials is nanocrystalline materials: polycristalline materials with a significant amount of crystal grains in the nanoscale. During the past decades, extensive research on nanocrystalline materials has been carried out, due to their peculiar mechanical and functional properties [21].

Processing of nanocrystalline materials presents various options such as solid-phase, liquid, vapor-phase and solution processing. The latter includes electrodeposition technique, which is extensively used for its versatility in the production of a wide range of materials with specific grain size, composition, foil thickness and purity [15][49]. Deposition parameters, such as current density, deposition technique, substrate, pH and additives of the electrolyte, have a remarkable influence on grain size of electrodeposits. It is actually nearly unfeasible to process pure and defect free foils and alloying has been proven to be an effective method to reduce grain size of electrodeposits [16].

In particular, in the last fourty years, the electrodeposition of Ni-Fe alloys has gained attention due to their potential application to microelectromechanical systems (MEMS) devices, magnetic devices, functional coatings, microsensors and microactuators because of their magnetic, thermal and mechanical properties [28][32][37]. Nickel and iron are completely soluble in each other and they can present both FCC (face centered cubic) and BCC (body centered cubic) crystal structure, depending on whether

it is a nickel or iron-rich alloy [33].

Moreover, the amount of iron deposited with nickel strongly influences grain size and texture, hence mechanical properties. Speaking in terms of ultimate tensile strenght (UTS) and Young's modulus, it has been found that they both decrease with increasing iron content [26] [30].

Furthermore, with decreasing grain size an increase in hardness can be witnessed, according to the Hall-Petch law. However, for grain size around $18nm$ and smaller, an inverse Hall-Petch behaviour was observed [27] [31] [43]. The same behaviour has been found in pure nanocrystalline Ni and other nanocrystalline metals. The transition from regular to inverse Hall-Petch behaviour has been studied extensively and different theories have been presented [8], involving various contributing factors, such as pile-up [38] [39], annealing [45], texture and diffusional creep [12].

Creep in nanocrystalline Ni-Fe alloys is presently a controversial issue. The concept of creep itself is linked to the response of a material to the application of a constant load. Such response is an increasing time-dependent viscoplastic deformation. Hence the mechanisms involved in creep are different from the ones witnessed in plastic deformation only. Creep mechanisms can be both dislocation based, such as cross slip and climb with respectively screw and edge dislocations, and non dislocation based, such as diffusion and grain boundary sliding (GBS). Moreover,creep can have a significant impact on measurement of hardness and Young's modulus values through nanoindentation tests [34]. Also, first studies about indentation creep were carried out with conventional hot hardness tests at high temperatures, without recording a load-displacement curve [36].

Nanoindentation is a variety of indentation hardness test performed on small volumes. It does not require any sample preparation and it is the fastes way to measure mechanical properties of a wide range of materials. These tests have also proven effective in the estimation of tensile properties, instead of relying only on tensile tests [22]. During the test both load and penetration depth are continuosly monitored and, when the indenter is withdrawn from the specimen, a residual impression is left and its corresponding residual penetration depth is measured. A load-unlod curve is obtained with respect to indentation depth and mechanical properties can be evaluated [6] [41]. Both loading time and hold period are key factors in the evaluation of such properties, but the effects of the latter have been considered negligible if reccomended values of hold time are used [13]. Moreover, also at room temperature, creep and thermal drift effects can be significant when peak load is reached and a correction should be adopted [19]. Main issues of nanoindentation creep tests are due to sharp tip indenter geometry [4] and the difference between indentation creep and the conventional uniaxial creep testing. Such problems could be solved by adopting spherical indentation creep and pillar compression creep testing, yet not commonly used [11].

It is crucial, in any case, to investigate sample microstructure and to consider the conditions of deposition as well as heat tratment history of the latter. It has been found that additives, such as saccharine, yield to a reduction in grain size and to an increase in dislocation density [23]. A rise in dislocation density can be achieved through annealing as well [7]. Moreover, due to the presence of additives, the structure can result homogeneous and do not show any texture within the foil thickness [23]. It is important to notice that Ni-Fe alloy films usually present a columnar structure, made of so called columnar grains. Each of them is composed of medium sized grains, around $150nm$, called characteristic grains, which contain nanocrystalline grains, up to $10nm$ in size (fig. 1.1, [29]).

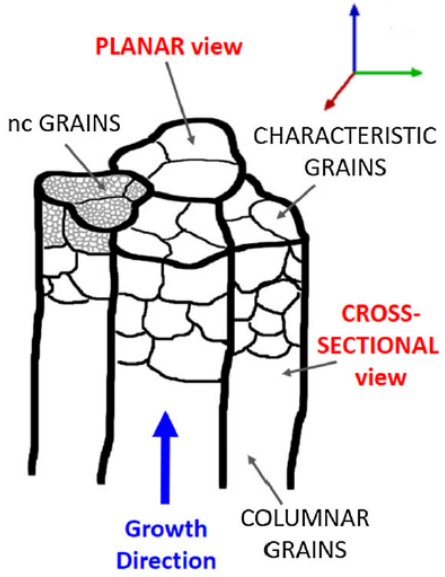

Figure 1.1: *Scheme of electrodeposited Ni-Fe alloy structure*

The behaviour of such materials during nanoindentation tests has been investigated with numerical simulations, as well. In particular 2D models with conical indenters have been proposed [17] and 3D models with axialsymmetric indenters, such as Vickers [47], which gave the possibility to partialize the problem and study only one fourth of it.

This work focuses on the study of electrodeposited Ni-Fe alloys both annealed and as-deposited by means of chemical, microstructural and nanoindentation tests. Specifically, nanoindentation test have been performed with a Berkovich indenter, which is not axialsymmetric. A numerical simulation is proposed, with geometrical adjustments to allow the study of one sixth of the model.

2 Samples preparation

The analyzed foils were produced by electrodeposition processing. An AISI 304 stainless steel and Ni plates have been used as electrodes, respectively as cathode and anode. The elctrolyte bath contained iron chloride, nickel sulphamate, boric acid, ascorbic acid and saccharine, added as grain refiner and stress reliever. The process has been conducted under direct current DC condition. A Ni-Fe film was deposited over the cathode and then mechanically removed to obtain a foil. More detailed information about the deposition process can be found in ref. [25].
Specifically four foils have been considered (fig. 2.1):

- 46-53 Ni, thickness 200μm as deposited,
- 52-55 Ni, thickness 100μm as deposited,
- 50-54 Ni, thickness 45μm as deposited,
- Ni- 48Fe, thickness 200μm and heat treated at 370$^{\circ}C$.

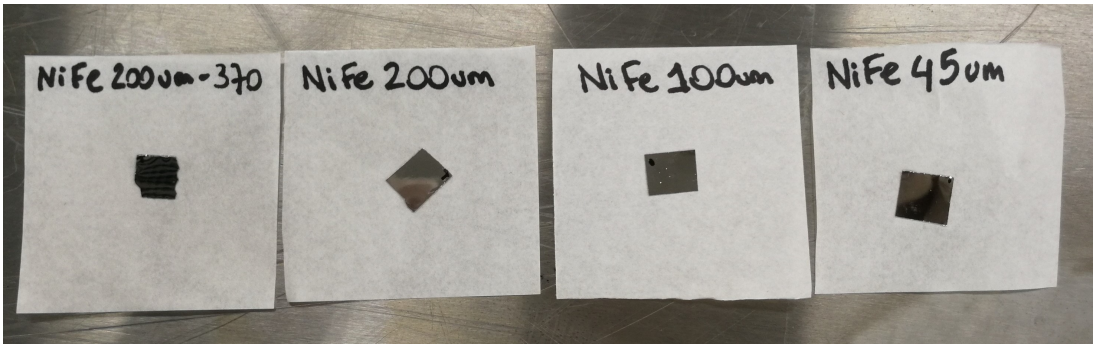

Figure 2.1: *DC electrodeposited Ni-Fe foils*

Each sample can be thought as a plate element in which a top surface and a cross section surface can be identified as shown in figure 2.2.

It has been necessary to carry put experiments on both surfaces so two different mounting procedures were used.

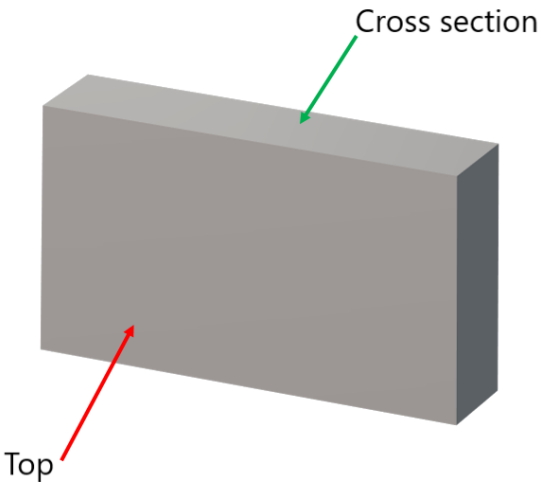

Figure 2.2: *Sample geometry*

2.1 | Mounting with epoxy glue

In order to operate on the top surface, each sample has been fixed to a metal support through epoxy glue. At first samples were mounted using white glue. This choice proved to lead to non reliable results during nanoindentation tests due to the small thickness of the samples and the non homogeneous distribution in the layer of glue. In the end a total of four samples of the kind shown in figure 2.3 has been obtained.

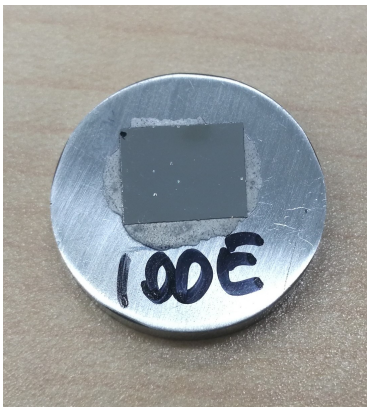

Figure 2.3: *Sample mounted with epoxy glue - investigation on top surface*

2.2 | Mounting with epoxy resin

To carry out investigations on the cross section surface, it was necessary to clamp the foils in such a way that the cross section was parallel to the horizontal working plane, hence the top surface was made perpendicular to said plane. This structure has been placed in a mould, prevoiusly covered with a no-stick liquid (fig. 2.4).

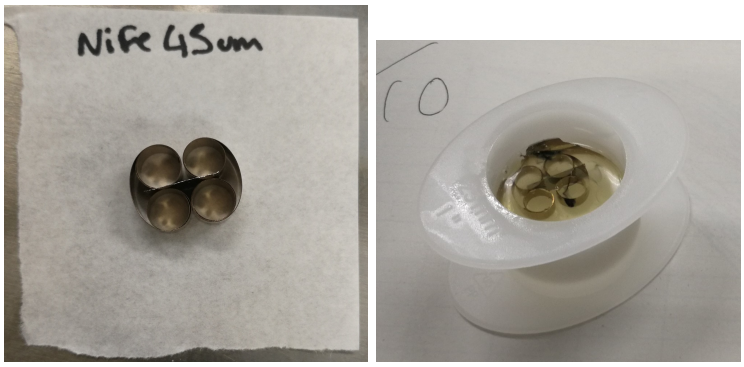

Figure 2.4: *Preparation of sample for epoxy resin mounting*

The epoxy resin is made by mixing resin and hardner. Proportion is fixed and can be calculated based on the number of samples to produce. Once dry, the newly formed sample (fig. 2.5) has been extracted from the mould and polished to a mirror finish. Sandpapaer from very fine to ultra fine micro mesh size and colloidal silica polishing suspension as last step have been employed.

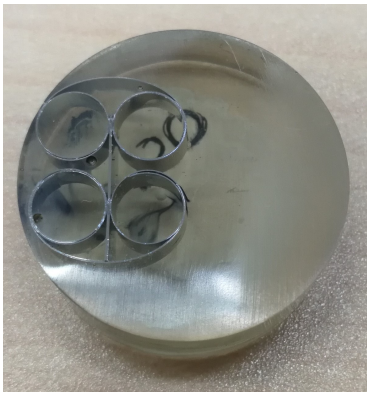

Figure 2.5: *Epoxy resin mounting*

Mechanical characterization

3

3.1 | Hysitron TI 950 TriboIndenter

A Hysitron TI 950 TriboIndenter nanomechanical testing instrument equiped with external vibration detector (top right in figure 3.1) and its dedicated softwares Hysitron TriboScan and Hysitron TriboView have been used to perform and analyse nanoindentation tests and study the surface of the samples, both top and cross section.

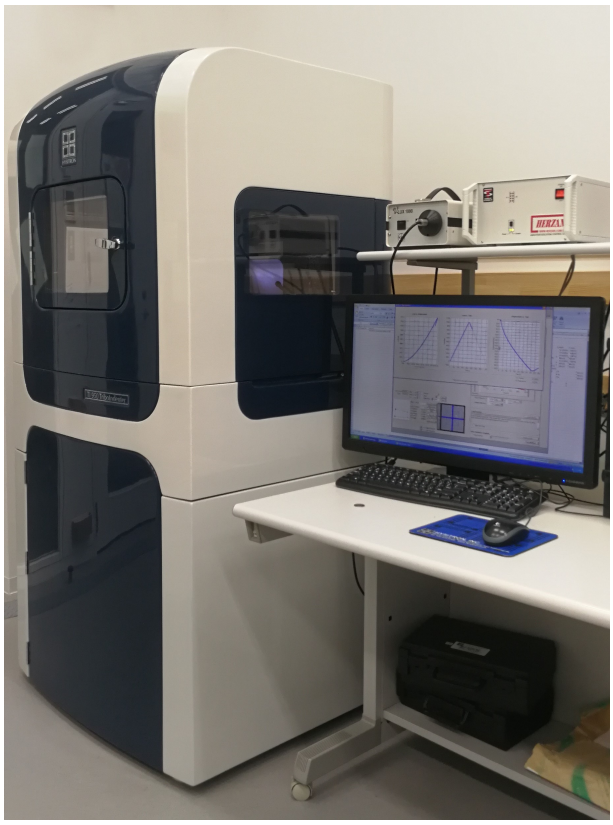

Figure 3.1: *Hysitron TI 950 TriboIndenter- work station*

The software interface is organized in various tabs:

- *sample navigation tab* to control the stage and set the boundaries of the sample;
- *load function tab* to set the load function to be used in the tests;
- *analysis tab* to visualize the obtained load-displacement curves;
- *imaging tab* for in-situ scanning images;
- *automation tab* to set tests to be performed at imposed location on the sample, following a given geometry pattern;
- *calibration tab* to ensure the right setting of the instrument.

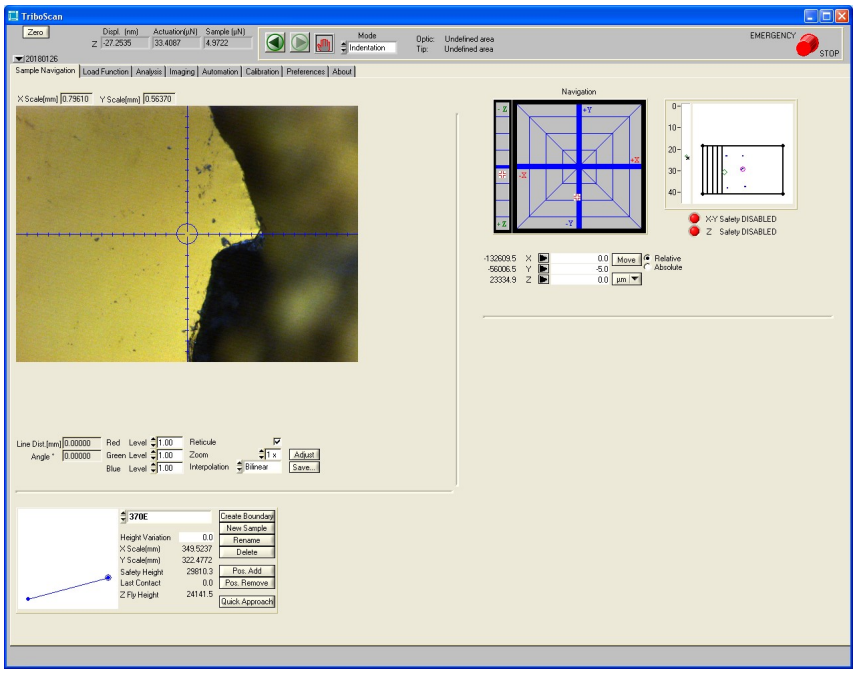

Figure 3.2: *User interface during boundary definition of new sample*

3.1.1 | SPM imaging

The instrument is equiped with a scanning probe microscope (SPM) which is able to form an image of the surface of the specimen by scanning it with a probe. All the pictures obtained for this work have been adjusted with an average plane background subtraction method, which means that any tilt effect has been removed by the software considering the whole image and no artifact is introduced. This technique ensures well balanced images, but it is not available during real-time scanning. Regarding in-situ scanning, four images are saved for each area of interest:

- two topography images: forward and reverse direction;
- two gradient images: forward and reverse direction.

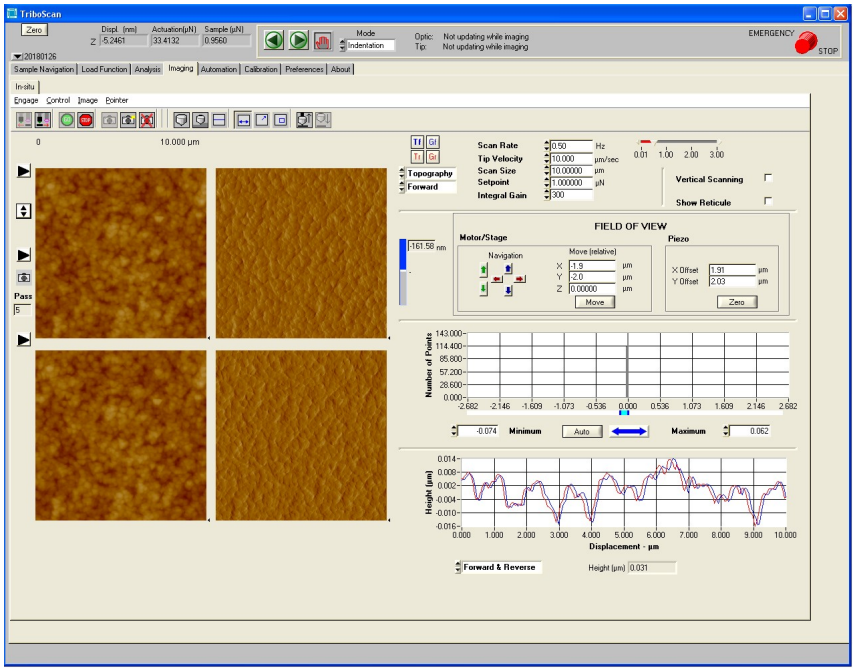

Figure 3.3: *User interface during in-situ imaging on top surface of heat treated sample*

3.2 | Nanoindentation test

The tests have been performed with different load functions, which can be divided in groups by considering peak load, loading rate and hold time. Specifically, three peak loads have been tested:

- $1mN$;
- $5mN$;
- $10mN$.

Load and unload rates have been set symmetrically at first, with the following values for each peak load:

- $5\mu N/s$ only for $1mN$ peak load;
- $50\mu N/s$;
- $500\mu N/s$;
- $5000\mu N/s$

Hold time has been set to $30s$, $60s$ and $180s$. Further tests have been performed with an intermediate hold at load segment for the lowest peak load.

To perform a test, the sample has to be introduced in the machine and secured on

the stage, then it is possible to define its boundaries through the software. A load function needs to be set and a point in the previously defined domain has to be chosen. When the test starts, the indenter will move along the z-axis,perpendicular to the surface of the stage and specimen as defined in the user manual, and will approach the sample on the stage. Values for relative modulus of elasticity, hardness, area of deformed region, depth of indentation and thermal drift are measured and recorded by the system.
Data collected in this way have been analysed considering a Gauss distribution of the measured values of relative modulus of elasticity, hardness, depth of indentation and thermal drift.
In particular, the effects of thermal drift on the experiment were not negligible. Hence, all the measurements corresponding to a recorded thermal drift value not included in a ± 0.2 range were excluded. Moreover, in order to choose the most representative tests, standard deviation of relative modulus of elasticity and hardness have been calculated. In the end, the most representative tests have been considered the ones which lay in a range of $\pm$ *one standard deviation* of considered data, e.g. relative modulus of elasticity.

Tests have been performed on the top surface of each sample, first. The sample surface has been investigated through SPM in-situ imaging. In figure 3.4 at page 18 a square region of top surface with $10\mu m$ side is analyzed. The 3D rendering image is representative for the average roughness of the sample, which was considered suitable for automated tests.

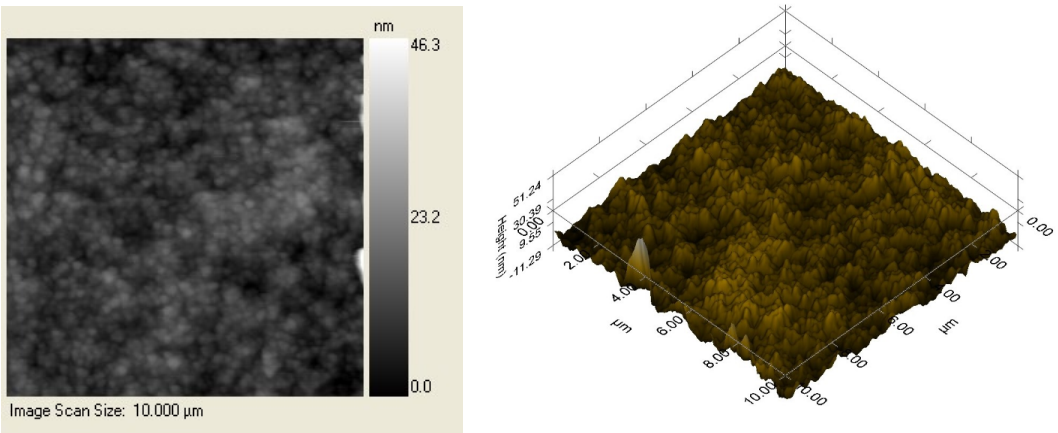

Figure 3.4: *SPM in-situ imaging of top surface (*$100\mu m$ *thickness sample): as scanned and 3D rendering*

Consequently, a $10x10$ grid of points has been initialized in the software. The spacing between two consecutive points and two consecutive lines of points has been set equal to $5\mu m$, because it is the smallest value that ensured no contamination among the tests.

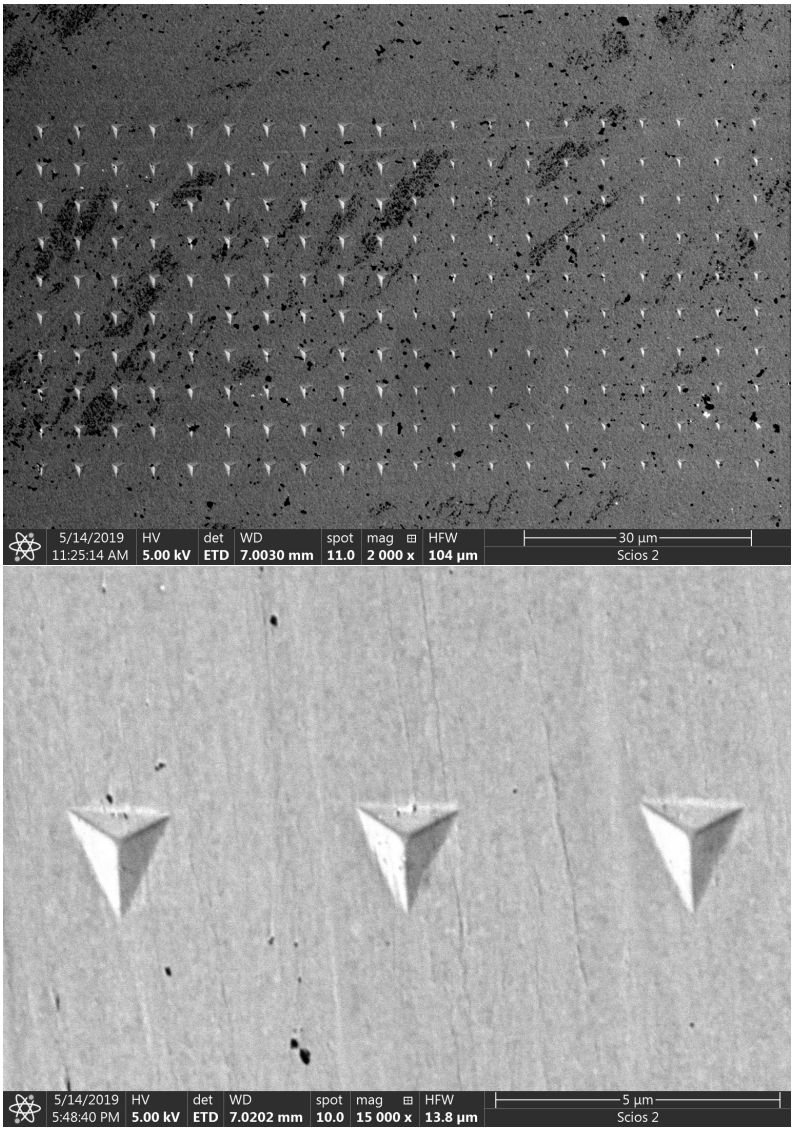

Figure 3.5: *Grid of automation: tests with* $10mN$ *preak load on the left,* $5mN$ *on the right Distance between two consecutive tests*

The relative elasticity modulus measured values E_r can be related to Young's modulus with the following equation:

$$\frac{1}{E_r} = \frac{(1-\nu^2)}{E} + \frac{(1-\nu_i^2)}{E_i} \tag{3.1}$$

where

- ν is the Poisson's ratio of tested material,
- ν_i is the Poisson's ratio of diamond, material of which the indenter is made,
- E is Young's modulus of tested material,
- E_i is Young's modulus of diamond.

To compute Young's modulus value for the tested material, ν has been assumed equal to 0.3 and the following equation has been used:

$$E = \frac{1-\nu^2}{\frac{1}{E_r} - \frac{1-\nu_i^2}{E_i}} \tag{3.2}$$

Moreover, relative elasticity modulus measured values showed a lower mean value for higher loads. It could have been due to the possibility of an hardness gradient on the thickness of the sample, so tests have been performed on the cross section side, with the epoxy resin mounted specimens, in line from top surface to bottom surface.

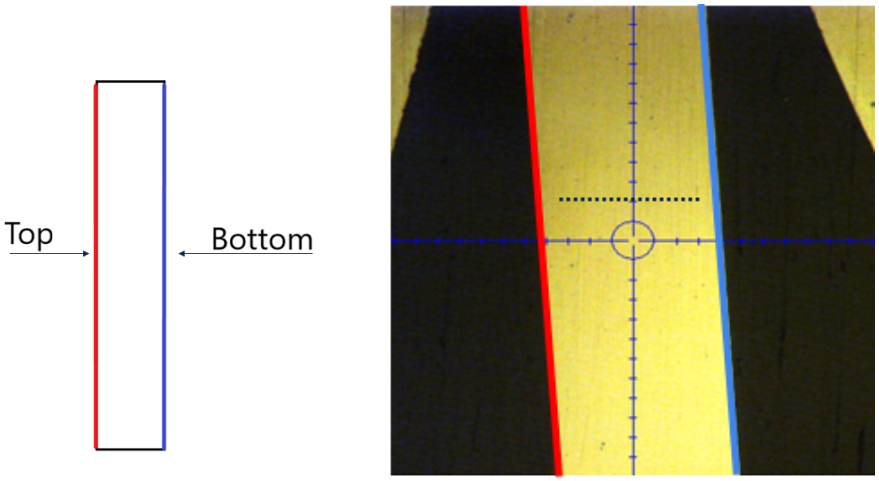

Figure 3.6: *Setting of nanoindentation tests on cross sectoin surface*

4 Chemical and microstructural characterization

4.1 | Microscopes

Electron microscopes uses the interaction between high voltage electron stream and the sample to create images, in a similar fashion as optical microscopes use light. The resolution of such instruments depends on the wave length of the used particles, hence, being the wave length of an electron much shorter than the one of photons, the electron microscopes have remarkably higher resolution. The two most common types of electron microscopes are:

- Scanning Electron Microscope SEM, used to investigate surface morphology and it is based on scattered electrons (fig. 4.1);
- Transmission Electron Microscope TEM, requires dedicated thin samples, extracted with FIB procedure and it is based on transmitted electrons (fig. 4.2, [42]).

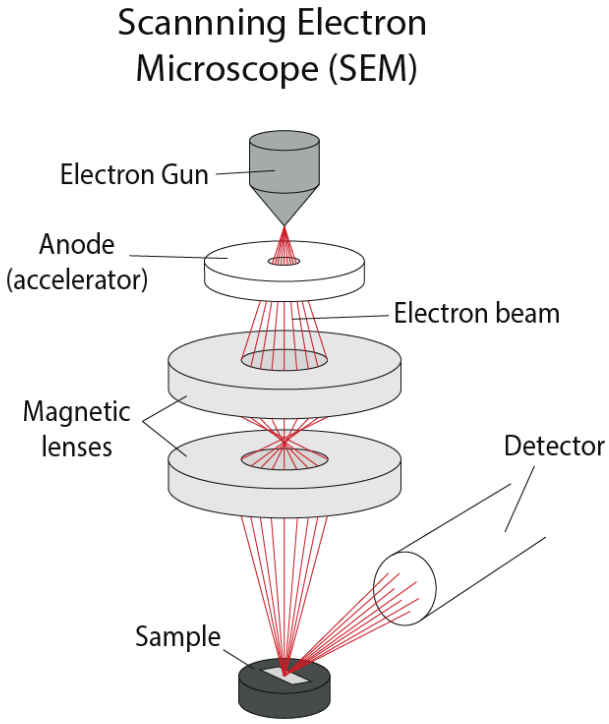

Figure 4.1: *Scheme of a scanning electron microscope SEM*

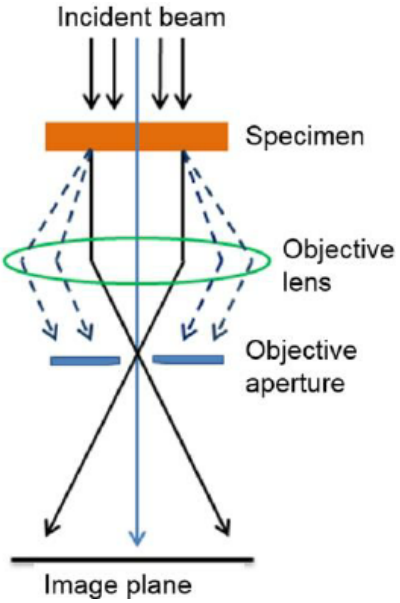

Figure 4.2: *Transmission electron microscope TEM: scheme of working principle*

4.1.1 | Scanning Electron Microscope -SEM

The Scanning Electron Microscope *JEOL JSM-7200F* has been used to observe the top surface of the heat treated sample. Electron stream was set to 20*kV* and the working

distance (WD), the distance at which the beam is focused, was equal to 16mm. The first image obtained is shown in figure 4.3.

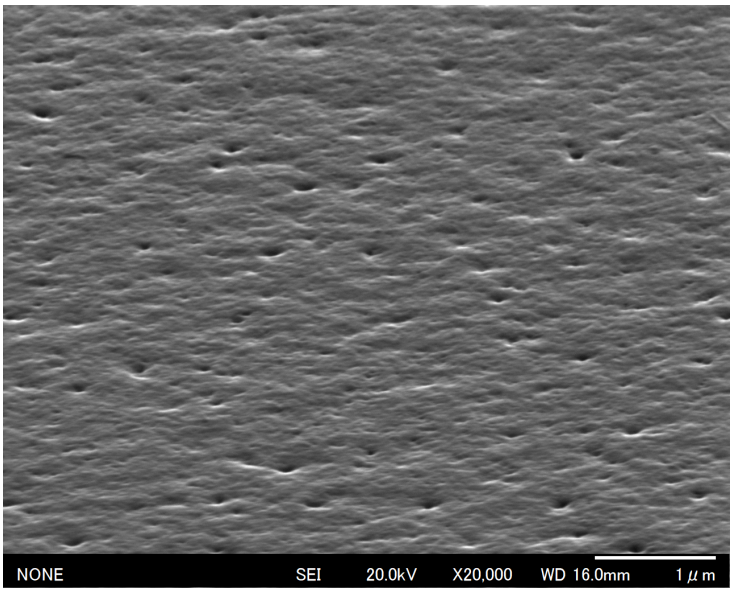

Figure 4.3: *First attempt to observe heat treated sample top surface with SEM*

Zeiss Auriga instrument has been used to perform further investigation on the cross section surface of the sample with 200μm thickness, as deposited. It has been analysed twice:

- as polished and cleaned with liquid alconox[1]
- surface with Osmium coating, for stability reasons.

In the first case electron high tension (EHT), the voltage through which the electrons were accelerated towards the specimen, was set to lower values ($0.5 - 2kV$) compared to the second case ($5kV$). The difference can not be ascribed to a general rule, but it is common practice to work with lower accelerating voltages when the sample has not been coated. The choice of the values of the parameters depends on various factors and it is strongly influenced by the presence of drift (keeping the sample in focus is challenging because it moves continuously) when setting the specimen in the machine. In particular, when working with epoxy resin mounted samples, the contrast of the image can be not high enough, resulting in a shiny image in correspondence to the material section. For this reason, carbon tape (fig. 4.4 at page 24) can be applied to the sample to create a dark frame around the area of interest in such a way that the focusing and setting procedures become easier. Copper tape was used as well to make FIB focusing easier.

[1] anionic detergent for manual cleaning, free rinsing

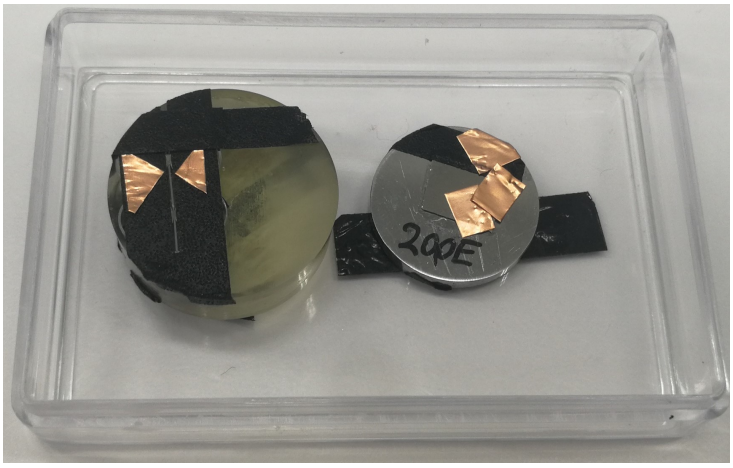

Figure 4.4: *Application of carbon and copper tape*

4.1.2 | Transmission Electron Microscope -TEM

JEOL JEM 2010F has been used for observation of lamellae extracted from top surface and cross section of 100μm thickness foil, as deposited and 200μm thickness, as deposited one. Moreover, samples have been extracted both before and after nanoindentation tests to find differences in the region underneath the indenter and compare it to an undeformed one. Diffraction patterns have been obtained and a face centered cubic FCC crystalline system could be qualitatively identified, by observing the distance between the diffraction rings representing (111) and (200) planes.

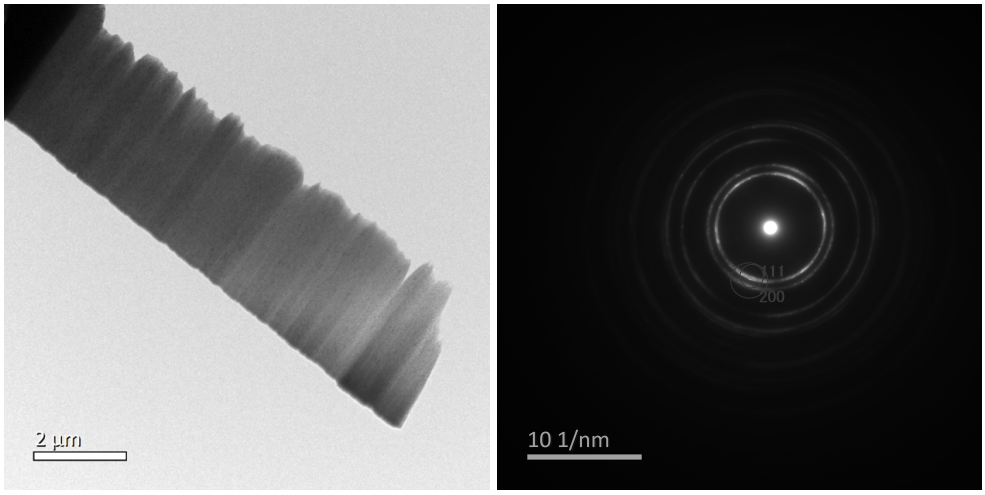

Figure 4.5: *Lamella extracted from* 200μm *thickness, ad deposited sample and diffraction pattern*

JEOL JEM 2800 has been used to perform EDS and EELS analysis.

4.2 | Techniques

The microscopes have been used for observation and for Focused Ion Beam sample preparation (FIB), Energy-dispersive X-ray spectroscopy (EDS), Electron Backscatter Diffraction analysis (EBSD) and Electron Energy Loss Spectroscopy (EELS) as well. These techniques work with different methods on the mechanisms of interaction between an electron beam and the specimen. In detail, second, backscattered, transmitted electrons and X-rays are used, as shown in figure 4.6.

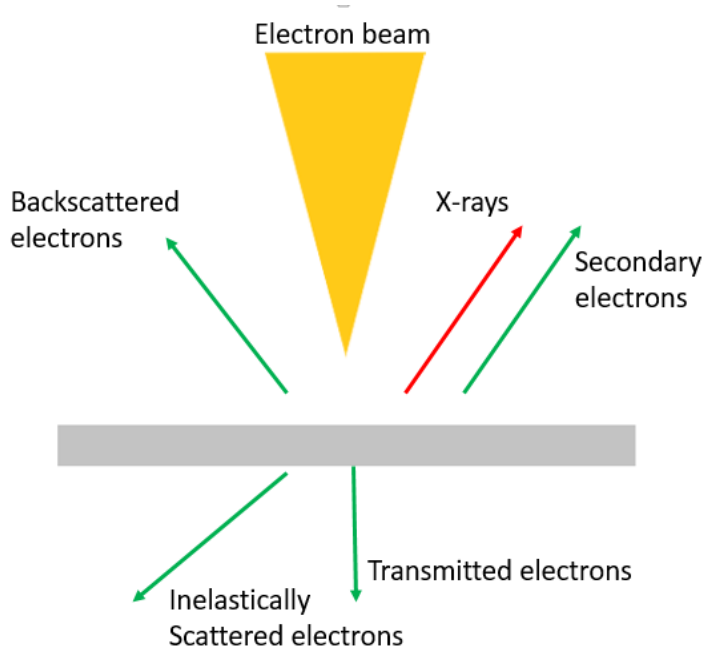

Figure 4.6: *General idea of working principles of most common SEM-TEM investigation techniques*

4.2.1 | Focused Ion Beam sample preparation -FIB

In TEM, it is necessary to use specifically designed samples to comply with the working principle of electron transmission of the instrument. For this reason, focus ion beam (FIB) sample preparation is used. Five samples have been extracted with *Thermo Scientific Scios 2 DualBeam* from four specimens:

- 200μm thickness, as deposited, top surface;
- 200μm thickness, as deposited, top surface with indentation mark;
- 200μm thickness, as deposited, cross section surface;
- 100μm thickness, as deposited, top surface;
- 100μm thickness, as deposited, cross section surface;

Figure 4.7: *Thermo Scientific Scios 2 DualBeam*

The sample is placed on a support and it is put inside the machine where it is hit by two streams coming respectively from the focused ion beam and the electron beam of SEM, the two beams are placed at a relative angle of 52°. Together with the sample, a lift-out grid is secured in the machine: it will be used as support for the extracted lamella.
Once the machine has reached the internal working condition, the procedure starts with focusing operation. They consist of the tracing of rectangles and X signs. The sample is in focus when such signs are coherent and clearly marked. Examples of both successful and unsuccessful focusing steps are provided in figure 4.8.

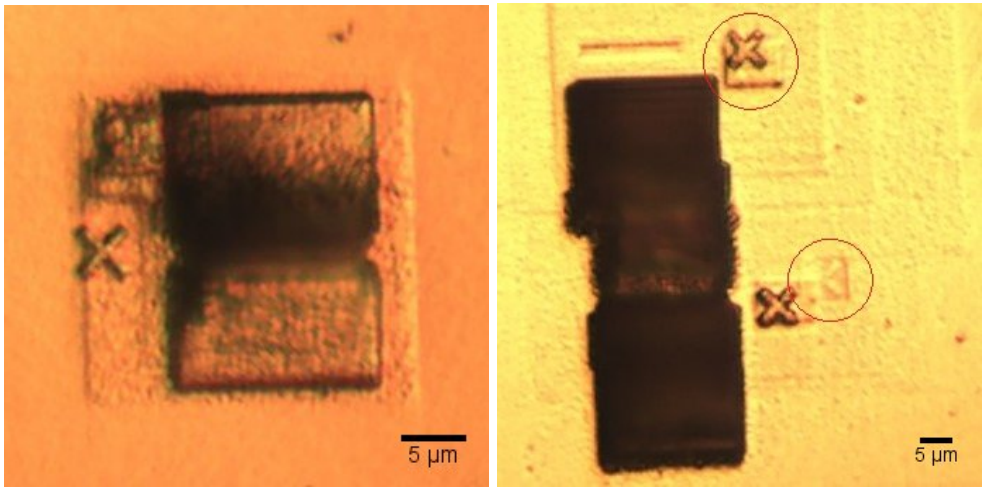

Figure 4.8: *Attempts of focusing in FIB sample preparation*

The area of interest for the extraction of the lamella is highlighted by drawing a rectangle of desired dimensions. The rectangle is used to procede with platinum deposition in order to protect the material during the process.
A rough cut of two rectangular pockets,adjacent to the deposited Pt, is made by milling, perpendicular to the surface plane. Specifically, in figure 4.9, the lamella can be seen right after the milling phase, which left a clear view of the columnar grains.

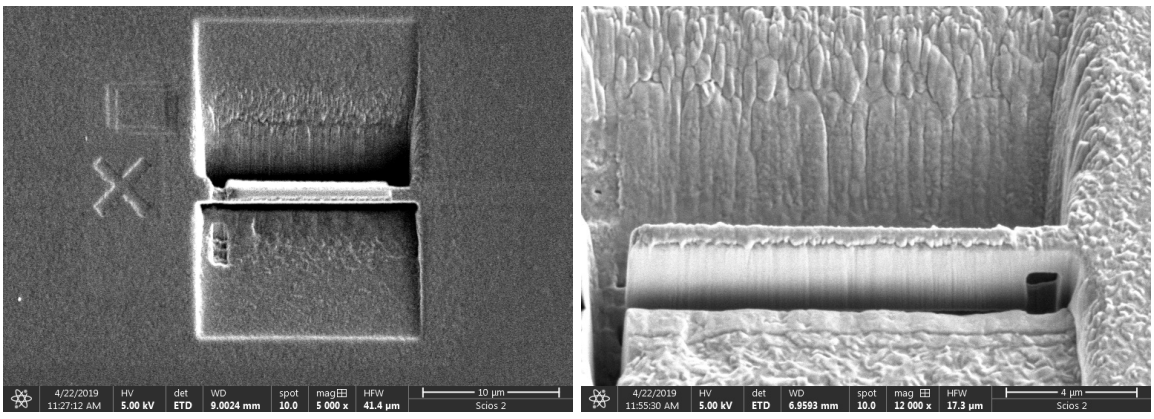

Figure 4.9: *Lamella extraction: Pt deposition and milling pockets*
Detail of lamella extraction: columnar grains

The final cut is operated and the lamella is moved by a micromanipulator solidal with the lamella by means of platinum contact. It is then attached to the nano-mesh, with platinum. Various types of lift-out meshes are available.

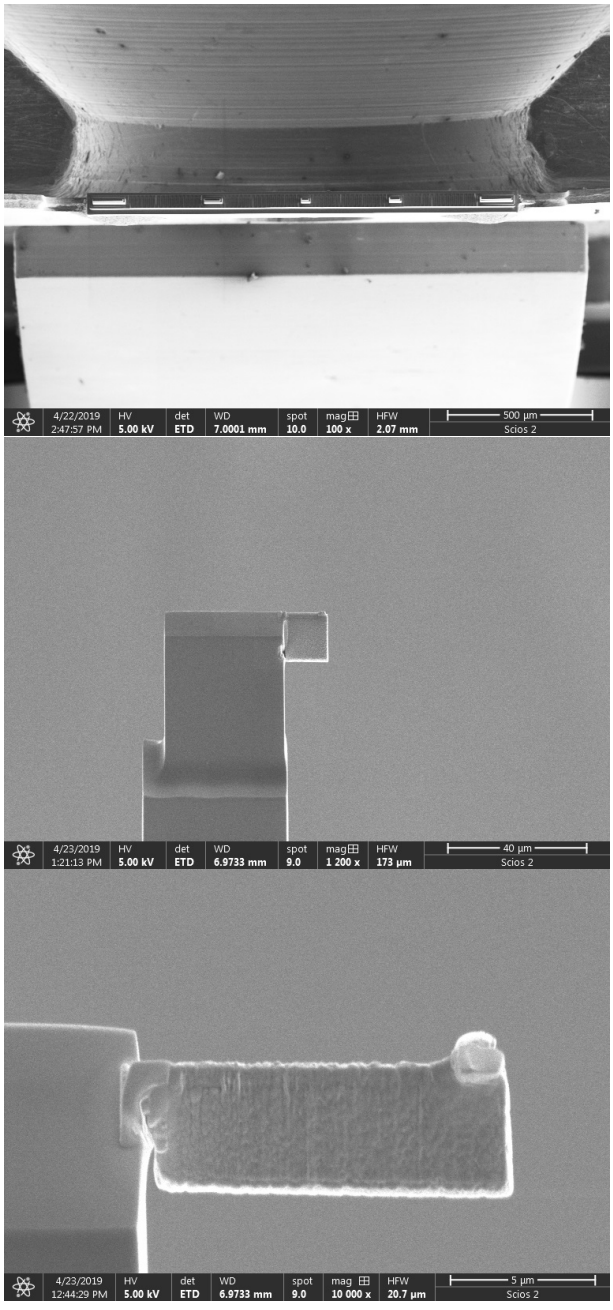

Figure 4.10: *Top view of TEM nano-mesh*
Front view with lamella attched
Detailed view of lamella, after extraction

Once the lamella is secured on the nano mesh, the final thinning is performed, followed by the cleaning at low voltage. The final thinning is the most delicate step:

the goal is to achieve a thickness value constant on all the lamella and low enough to make TEM observation more effective. A reliable feedback on the final milling is the transparency of the lamella. The milling is performed with prescribed values of tilt angle and ion beam current based on the residual thickness to work on. For thickness varying from $800nm$ to less than $100nm$, the corresponding values of ion beam current are from $1nA$ to $50pA$ respectively. Tilt angles depend on the milling side and in general they vary from $50.5°$ to $53.5°$. The auspicable final result, will look like the lamella shown from top view in figure 4.11.

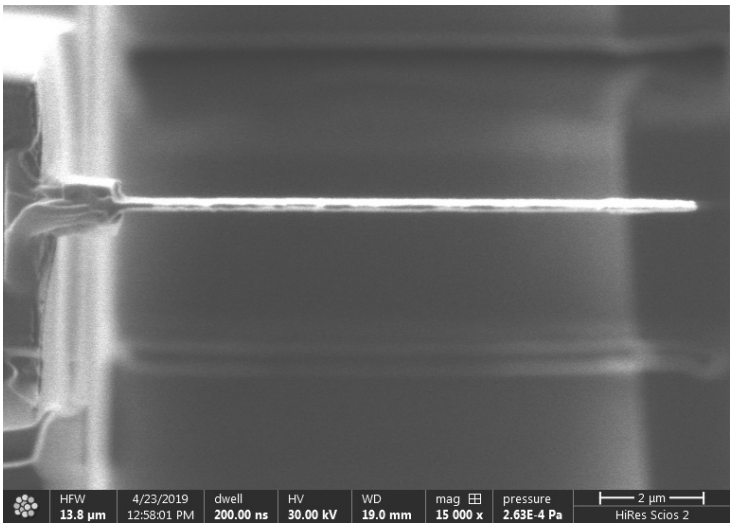

Figure 4.11: *Top view of lamella, after thinning*

The sample preparation procedure is crucial for further experimental activity and it can require a long time to be completed: it took two full working days to extract four lamellas. Especially when the aim is to extract a lamella from the cross section of an indentation mark, the chances of failure are very high due to the difficulties during thinning enhanced by the structure of the material. The procedure is the same already presented, but special attention has to be paid to preserve the section of interest. The indented specimen has been, then, covered with platinum and then marked with a segment like sign in correspondence to the indentation mark tip. This sign has been used as a flag during extraction and milling process (fig. 4.12 at page 30).

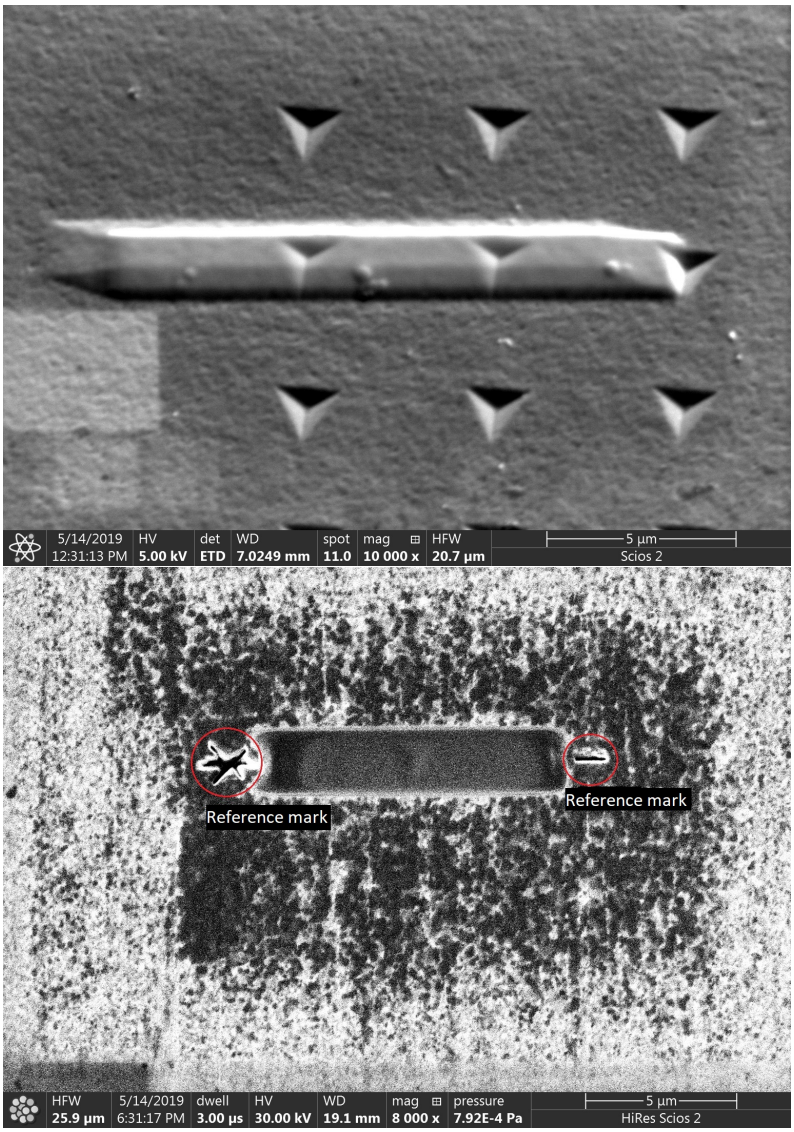

Figure 4.12: *Lamella extraction on indented specimen*

4.2.2 | Energy-dispersive X-ray Spectroscopy -EDS

Energy-dispersive X-ray spectroscopy is a chemical analysis and it can be performed in both SEM and TEM. It is based on the consequences of electron beam-sample interaction specifically in terms of X-rays generation.
The electron beam hits the sample and consequently it transfers some of its energy to the electrons of the specimen. The atomic structure of the sample is made of a nucleus and different shells to which it is associated a certain energy level (fig. 4.13). Moreover, every atom has a unique number of electrons with assigned position in the shells under unperturbed conditions. The absorption of the energy coming from the electron beam by the electrons of the specimen can lead to a jump to a higher energy level shell or an expulsion from the atom. In any case, the electrons create vacancies, which are associated with positive charge. The empty positions are filled by electrons belonging to higher energy shells. When it occurs, the energy difference between the shells can be released as X-rays. The energy of this X-ray is characteristic of the energy difference between the involved shells and it depends on the atomic number, linked to a single element.

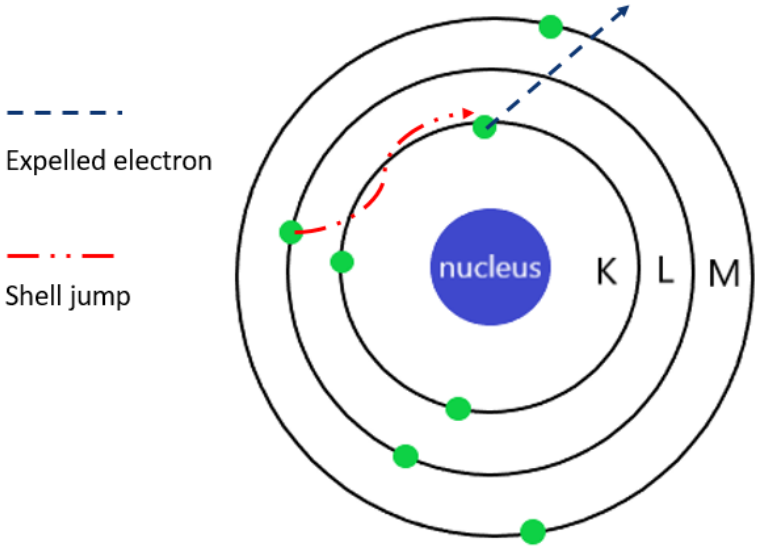

Figure 4.13: *EDS analysis working principle at atomic level*

The layout of the results is a spectrum with peaks corresponding to the elements that are present in the sample. EDS is considered both a qualitative and quantitative analysis.
EDS has been performed using SEM *Zeiss Auriga* and TEM *JEOL JEM 2800*. Results have been post processed with software *EDAX Genesis* and *OIM TSL*, *Gatan Micrograph* respectively.

4.2.3 | Electron Backscatter Diffraction -EBSD

Electron backscatter diffraction is a microstructural analysis operated with SEM. It has been performed using *Zeiss Auriga*.
In EBSD, a moving support carrying the specimen is tilted to an appropriate angle (usually 70° were reached with intermediate steps) to expose the crystalline sample to a stationary electron beam. The interaction of the beam and the sample involves not only the surface of the latter, but also a portion of volume underneath. In fact,the elastic scattering of the beam induces the electrons belonging to the sample to diverge from a point under the surface. Hence, crystal planes are influenced and Bragg's law (fig. 4.14) has to be considered:

$$n \cdot \lambda = 2d \cdot sin\theta$$

where:

- n is a positive integer,
- λ is the wavelenght of the incident wave,
- d is the distance between lattice planes,
- θ is the scattering angle, in this case it can be thought as the angle at which the electron leaves the sample.

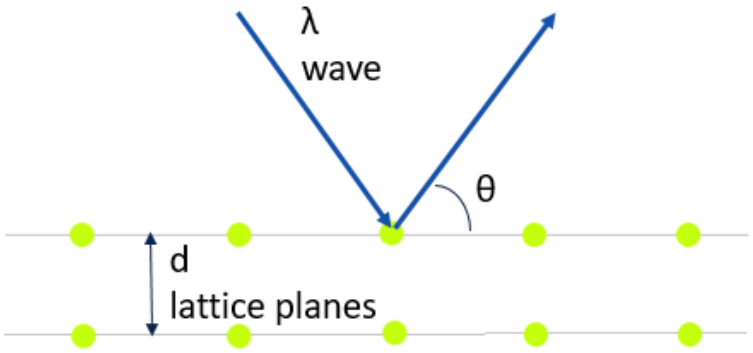

Figure 4.14: *Bragg's law*

The backscattered electrons which satisfy Bragg's Law for a given plane generate two diffraction cones, one above and one below the diffraction plane that can be identified in the specimen volume. Diffraction cones are produced for each family of lattice planes. The impression of two coupled cones on the phosphorus screen is two lines, which can be considered parallel and they form the so called Kikuchi band,

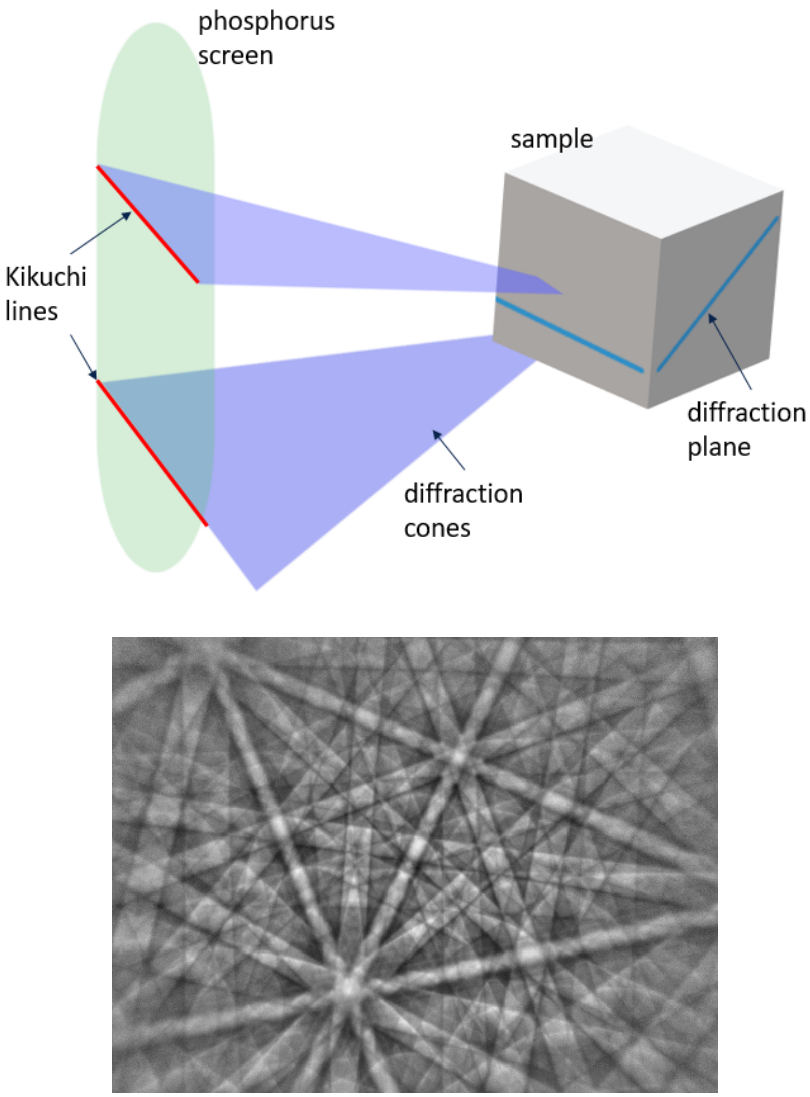

Figure 4.15: *From diffraction cones to impression of Kikuchi lines EBSP of Ni*

figure 4.15. The image formed is a diffraction pattern (EBSP - electron backscatter diffraction pattern[2]).

EBSD softwares store in a database the theoretical Kikuchi lines which are compared to the experimental ones. Using a matching algorithm, the lines in the pattern are translated in points to proceed with the mapping. An example of map is given in figure 4.16 at page 34.

Differnt colours on the map stand for different orientation. Such technique can be beneficial also in the investigation of grain boundaries and in the understanding of misorientation distribution.

[2]picture taken from educational site provided by Oxford Instruments

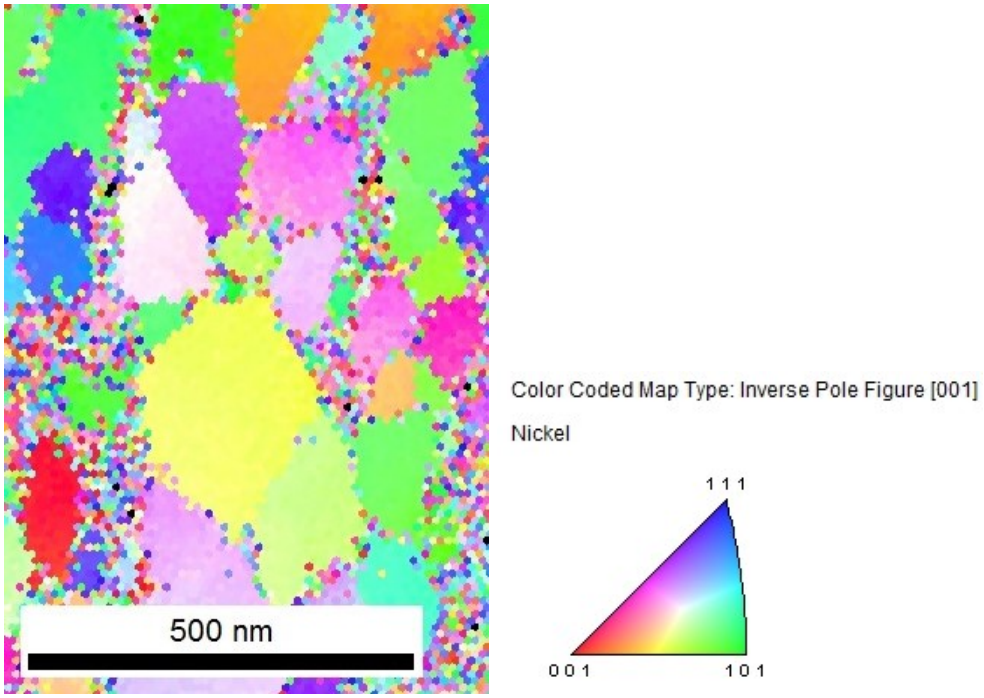

Figure 4.16: *Example of EBSD map with legend, as obtained with Zeiss Auriga*

4.2.4 | Electron Energy Loss Spectroscopy -EELS

Electron energy loss spectroscopy has the same goal of EDS, but it has higher sensitivity to most elements EELS is performed in TEM environment with thin specimens and it works with the inelastically scattered electrons. Inelastic scatter can be caused by inner shell ionization, namely the interaction with of the K, L, M shells. It is the most common type of inelastic interaction considered and a visual idea of the phenomenon is given in fig. 4.17. It means that in EELS, the signal considered is the one emitted by those electrons which have passed through the lamella and have lost a certain amount of their original energy. The value of the residual energy ΔE is given by the difference of the incident electron energy and the absorption energy of the sample.

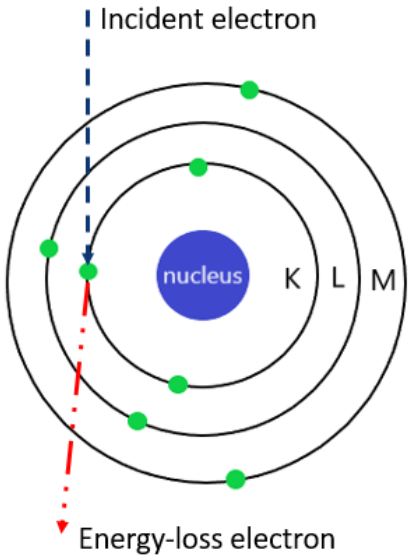

Figure 4.17: *EELS signal generation principle*

The values of ΔE can be linked to the energy required to remove inner-shell electrons from each element. EELS ionization edges are defined and compared to atom shells. Hence the result of an EELS analysis is a spectrum. Specifically, it can be divided in two parts:

- low-loss spectrum is up to 50eV in energy loss and it provides information about band structure and dielectric properties of the sample
- high-loss spectrum contain the peak values of the ionization shells due to the inner shell ionization in the sample and it provides information about elemental composition of the sample.

Computer simulation

5

To simulate nanoindentation tests, a 3D model has been developed using COMSOL Multiphysics 5.4, with Design module. The model is made by two main objects, called domains:

- Berkovich indenter;
- specimen with thickness $100\mu m$.

It is useful to introduce the concept of zero-plane, which is the plane parallel to xy-plane and containing the origin. It is the plane in which contact beetween indenter and sample is set to start.

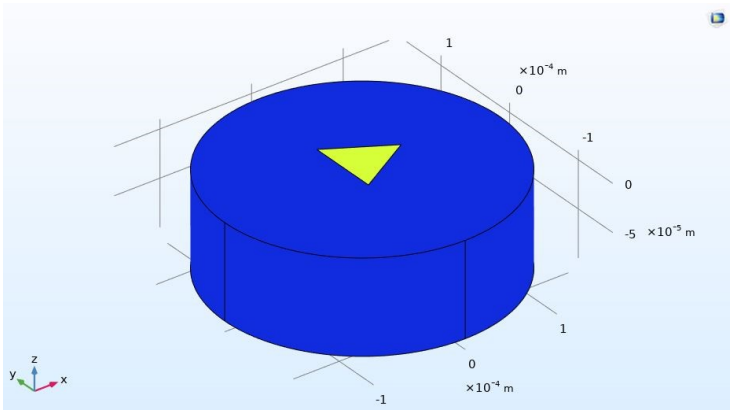

Figure 5.1: *3D model of nanoindentation test*

5.1 | Geometry

5.1.1 | Sample

The specimen has been modeled as a cylinder, with height $100\mu m$ at first. Due to the particular geometry of the Berkovich indenter, a new approach was implemented to optimize the computation.
Specifically, solely with the goal to simplify the model, two purely fictitious objects have been introduced:

- *inner cylinder*, modeled in correspondence to the contact point between intenter and sample;
- *tri-lobed region*, used to comply with the motion of the indenter during the test.

The latter has been thought in such a way that the central part contains the inner cylinder in all its length, while the lobes diminish in thickness from the center to the extremities. The planes used to cut this geometry are parallel to the sides of the indenter, consequently the tri-lobed region can be imagined as a housing for the indenter. The inner cylinder, shown in figure 5.2, has radius equal to $150 \cdot 10^{-9} m$ and height $280 \cdot 10^{-8} m$.

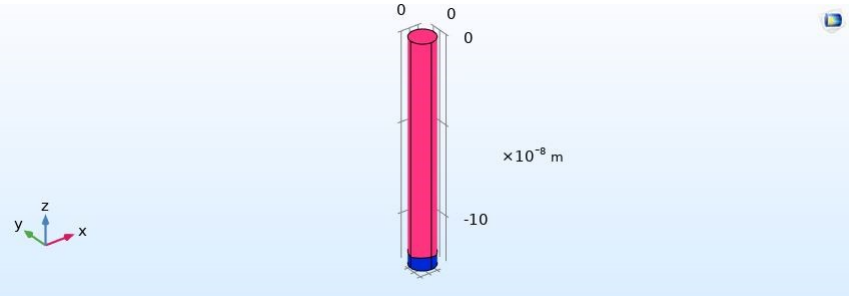

Figure 5.2: *Ficticious geometry: inner cylinder*

To obtain the tri-lobed region, as shown in figure 5.3, auxiliary planes and partitions of main domain were necessary. Specifically, 12 auxiliary planes have been used. The process can be split in two steps, namely tracing a tri-lobed region in the xy-plane and then creating a 3D geometry to realize the desired shape. For the first part, 8 planes have been used. Each lobe has $200 \cdot 10^{-8} m$ width obtained by setting this distance between the correspondent planes. To comply with Berkovich indenter geometry, one couple of planes is parallel to x-axis, while the other two couples are respectively parallel to two planes obtained by rotation around z-axis of $\pm 60.45°$. The first 8 planes are plotted in figure 5.4. For the 3D partition, 4 planes have been used: one is parallel to xy-plane and it has an offset equal to $280 \cdot 10^{-8} m$ from zero-plane, other three planes have been defined using spherical coordinates and in such a way that thickness of the region is maximum along z axis and equal to zero at the intersection with zero-plane. This procedure is shown in figure 5.5.

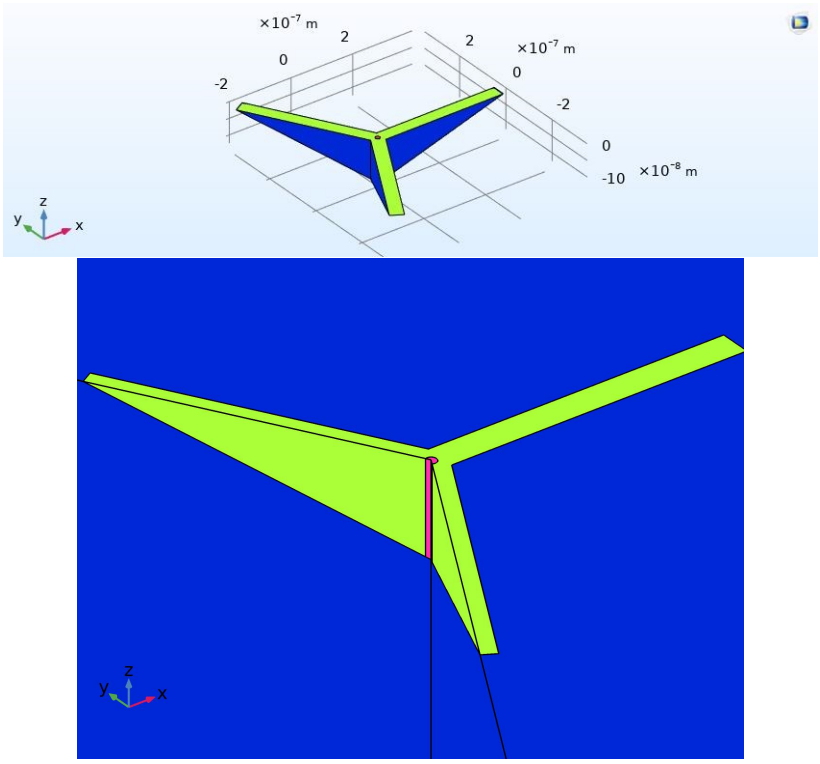

Figure 5.3: *Ficticious geometry: tri-lobed region*

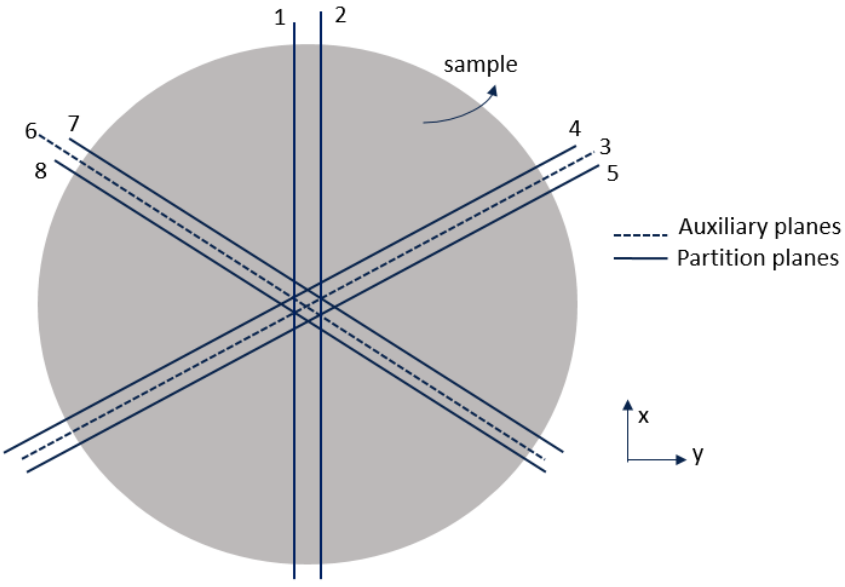

Figure 5.4: *Scheme of planes used to obtain the three lobes on xy-plane*

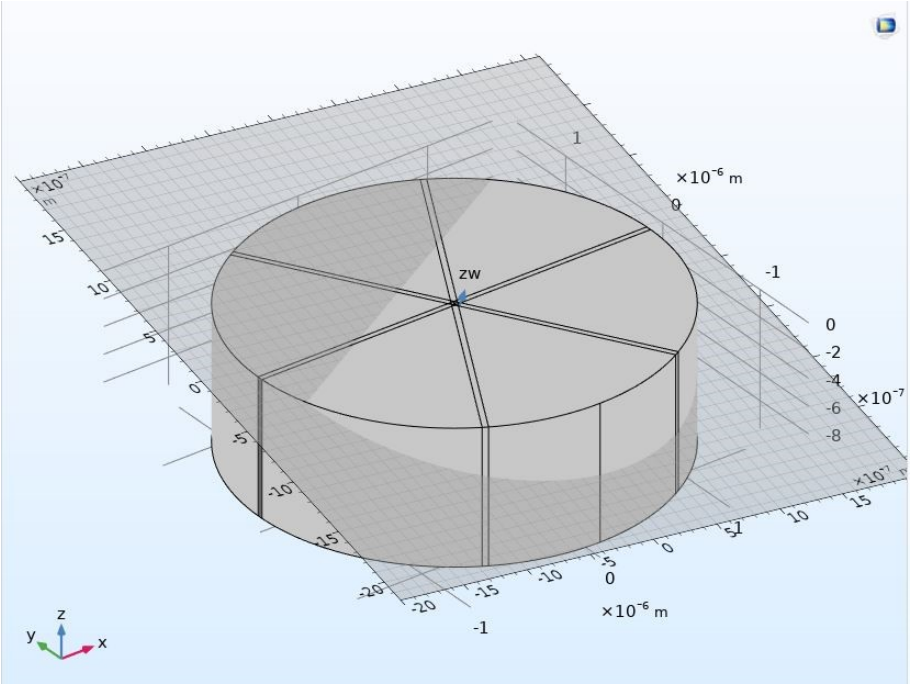

Figure 5.5: *Scheme of planes used to obtain 3D tri-lobed region*

5.1.2 | Indenter

The indenter has been modeled using a tetrahedron, which vertices coordinates have been computed in accordance to Berkovich indenter characteristic angles, namely 76.9° and 65.3° (fig. 5.6).
More attention has been drawn on the modelling of the tip. As reported in literature [9], the tip shows a round, sphere-like profile, which can be usually described as a sphere with radius equal to $150nm$ and tangent to the sides of the tetrahedron. A fillet feature, using COMSOL Design module, has been introduced in the model, not only at tip level, but also at edge level, in order to obtain a more realistic object. Actually such a value of radius is intended for a new tip, as produced. It is expected that the tip geometry and radius will change with usage. Fillet feature has a value equal to $30 \cdot 10^{-9}m$ (fig. 5.7).

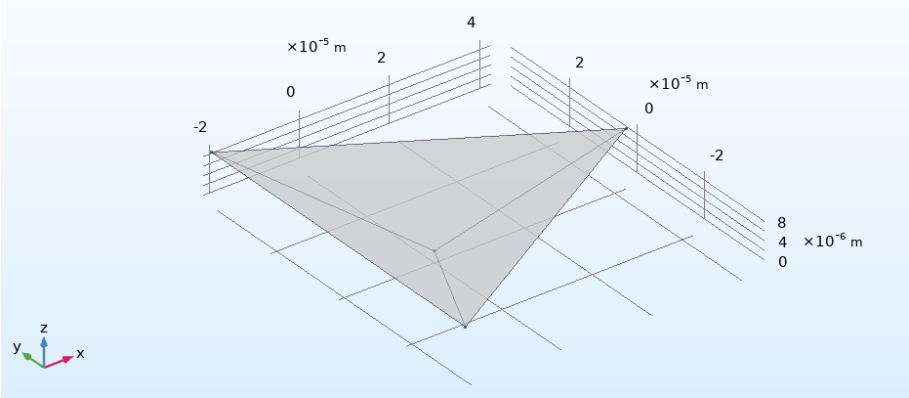

Figure 5.6: *Tetrahedron for Berkovich indenter*

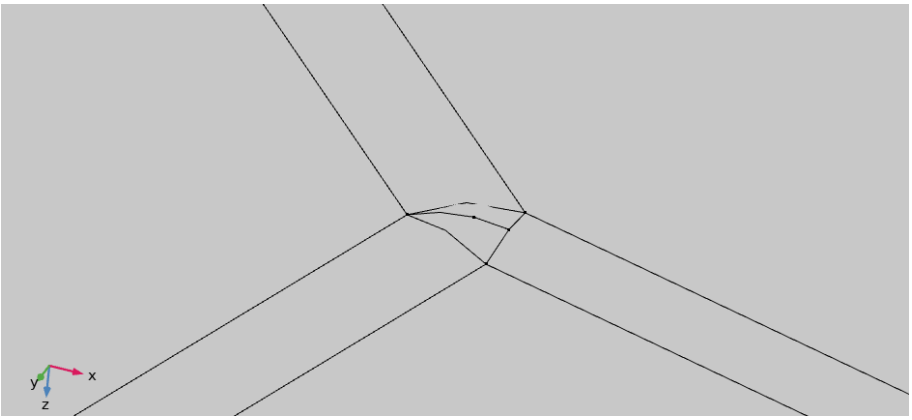

Figure 5.7: *Fillet on indenter tip*

The introduction of appropiate geometries in the sample, made the partialization of the model possible. Unlike in simulations with axial symmetric indenters, it would not be possible in this case to study just one part of the problem and consider it

reliable for the whole model, unless proper action is taken by using the tri-lobed region. The model has then been divided in six portions and only one of them has been used for computation, drastically reducing costs (fig. 5.8).

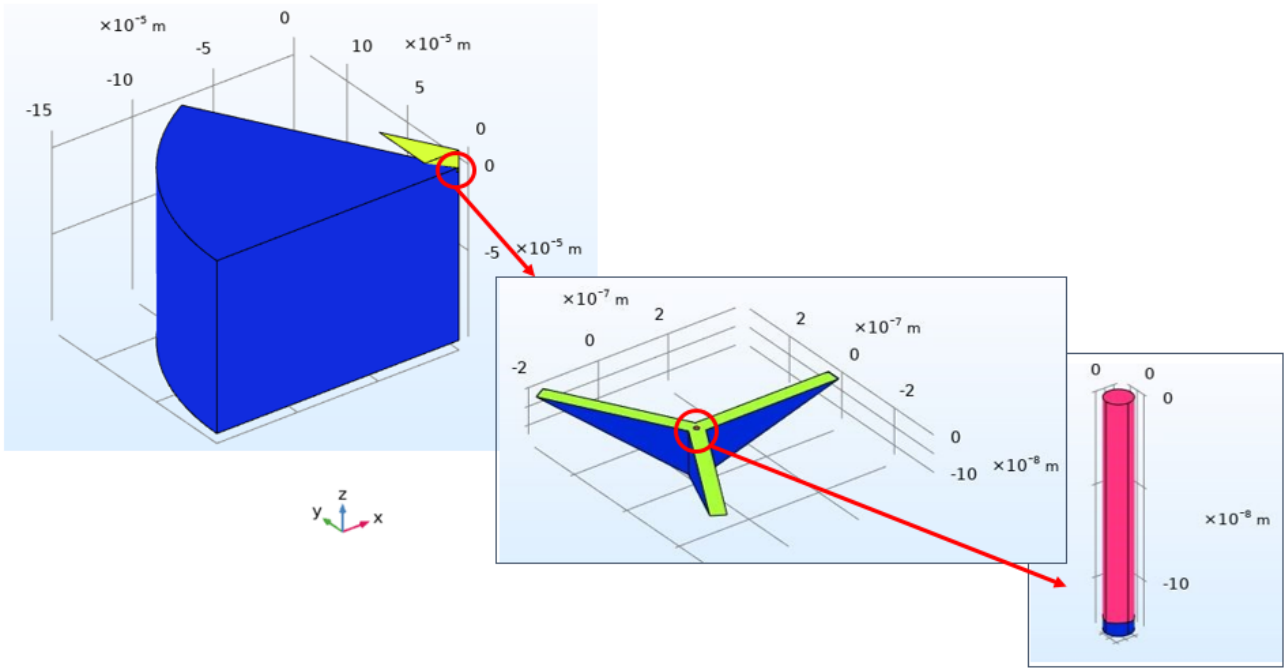

Figure 5.8: *Final adopted model geometry*

5.2 | Parameters and functions

Functions and parameters have been introduced to define both contact and load function. A non-dimensional parameter r has been considered as varying in a range from 0 to 50, with intermediate steps as shown in figure

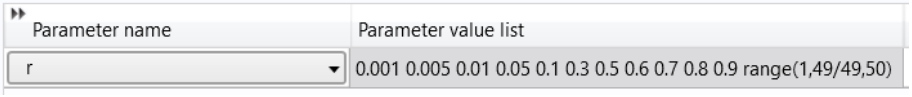

Figure 5.9: *Non dimensional parameter r range*

To model the load function L, a piecewise function has been defined, as function of parameter r and a constant value of force F, in three intervals:

- from 0 to 20
$$L = r \cdot \frac{F}{20}$$
- from 20 to 30
$$L = F$$
- from 30 to 50
$$L = (50 - r) \cdot \frac{F}{20}$$

The desired value of peak load F has been considered equal to $1mN$, but due to the reduction of the problem to one sixth of the whole model, also said values has been divided by six.

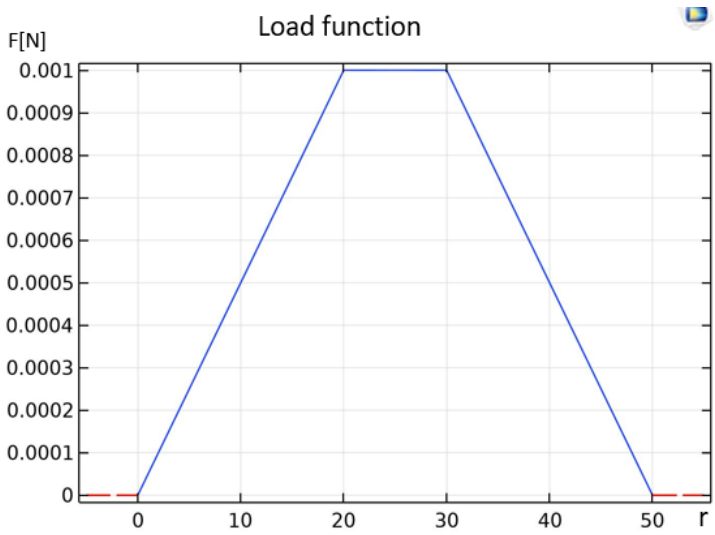

Figure 5.10: *Load function as piecewise function*

To model the contact between indenter and sample, a spring has been introduced to comply with the first steps of the computation. A piecewise function was defined, considering constant parameter k_0 and non dimensional parameter m, varying from 0 to 1, as follows:

$$K_{tot} = k_0 \cdot (1 - m) \cdot 2^{-10m} \tag{5.1}$$

5.3 | Materials

Materials have been defined for both indenter and sample. The indenter is made of diamond with following properties:

- Young's modulus: $1141 GPa$
- Poisson's ratio: 0.1
- Density: $3550 kg/m^3$

The sample is made of electrodeposited Ni-Fe with following properties:

- Young's modulus: $125 GPa$
- Poisson's ratio: 0.3
- Density: $8500 kg/m^3$

Properties of the sample partially come from experimental results and have been in part assumed, based on the properties of iron and nickel.

5.4 | Physical constraints

5.4.1 | Contact

It is fundamental to consider that the indenter and the sample are modeled as two different objects, hence to succeed in the simulation of the nanoindentation test contact between the two bodies has to be set properly. Specifically, COMSOL enables the user to define the contact among surfaces, which are either already in contact in initial configuration or will interact during the simulation. The two surfaces are called source and destination, in a similar fashion with whom they are called respectively master and slave in other softwares. In this case the source is the lateral surface of the indenter, while the destination is the top surface of the specimen. Contact has been modeled in such a way that the tip of the sphere of the indenter has coordinates $(0, 0, 0)$ like the center of the surface of the sample. This choice has been made to simplify post processing operations and setting of the simulation. Hence the zero position, so the position at which the interaction among the two objects starts, is set to be coincident with the origin of the global reference frame. To enforce the constraint two methods can be chosen:

- Penalty
- Augmented Lagrangian

Augumented lagrangian method needs the introduction of a new degree of freedom to record contact pressure. It is more robust than *Penalty method*, hence more expensive. For this simulation, Penalty method has been chosen. It is based on the idea of a spring connecting the two interacting bodies. The stifness of the spring is proportional to the penalty factor.Penalty factor should be large enough to ensure the enforcement of the constraint without causing ill-conditioning. The equation of the elastic force linked to the introduced spring foundation is

$$F_A = \frac{K_{tot}}{A} \cdot (u - u_0) \tag{5.2}$$

where K_{tot} has been defined by equation 5.1 only for the onset of contact, so when the adimensional paramenter varies from 0 to 1, and it is equal to zero for the rest of the test. The spring has been considered isotropic. Loss factor due to damping for the spring has been considered equal to zero and the contribution of viscous damping has been taken into account as constant per unit area and isotropic. The minumum distance which is interpreted as contact by the software for this application has been set equal to 10^{-15} due to the nanoscopic nature of the phenomenon to investigate.

5.4.2 | Other constraints

Berkovich indenter has been modeled as an elastic domain, with imposed displacement equal to zero both in x and y axis direction and imposed rotation equal to zero

around all three axis. In this way, the indenter can only move along z-axis direction. The bottom surface of the sample has been considered fixed. To lateral surfaces which are meant to be internal surfaces of the sample a symmetry condition has been imposed, while to the external surface a roller constraint has been imposed, which means that no displacement is allowed in any direction perpendicular to the surface. Top surface is free to comply with indenter motion. In the sample, plasticity feature has been set in accordance with the large plastic strain model, already implemented in the software. The yield function YF is

$$YF = \sigma_{mises} - \sigma_{ys} \tag{5.3}$$

While Von Mises stress is measured, yield stress is calculated with the formulation of isotropic hardening by Ludwick

$$\sigma_{ys} = \sigma_{ys0} + k \cdot \epsilon_p^n \tag{5.4}$$

where

- σ_{ys0} is defined by the user, equal to $300MPa$,
- k is the strenght coefficient, $725 \cdot 10^6$,
- ϵ_p is the plastic strain,
- n is the strain hardening coefficient, equal to 0.17 in this case.

Kinematic hardening has not been considered.

5.5 | Mesh and solver configuration

Finalized geometry has 2 domains, 7 boundaries, 13 edges and 9 vertices. Inner cylinder and tri-lobed region have been used as reference domains to set mesh requirements in the sample. When considering the contact indenter-specimen, it is useful to refer to the former as source and the latter as destination of the contact, as defined by the vocabulary adopted by the software. The destination mesh has to be at least twice finer than the source mesh which will be involved in the contact. Hence, it is handy to define a finer mesh in the inner cylinder domain, appropriate mesh in the tri-lobed region, corresponding to the edges of the intenter which will engage in indentation and coarser mesh in the rest of the domain representing the sample.

Specifically, to the outer circular edge of the inner cylinder a custumized mesh has been imposed, with maximum element size equal to $1nm$ and minimum element size equal to $0.3nm$. Other edges of the cylinder have been defined in a similar way with maximum element size equal to $5nm$ and minimum element size equal to $1nm$. Curvature factor and growth rate are the same in both cases, equal to, respectivelly, 0.2 and 1.3. On the other side the source of contact, the indenter edges, have been meshed with maximum element size equal to $300nm$ and minimum element size equal to $5nm$. Such dimensions of the mesh are useful to comply with the onset of contact which involves the specimen and the spherical tip of Berkovich indenter. Hence, the region of interest is much smaller than the complete model and moreover, the transition from spherical to planar contact is the most interesting part of the test for this study.

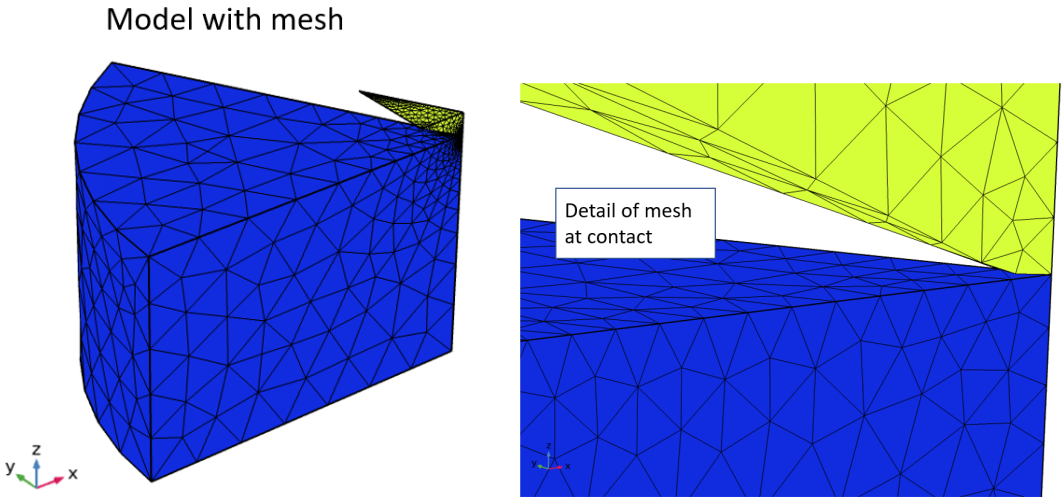

Figure 5.11: *Complete model with mesh, detail of mesh on the sample and at origin of global reference frame, contact point*

A multifrontal massively parallel sparse direct solver (MUMPS) has been chosen. It complies with symmetric positive definite matrices, general symmetric and unsymmmetric matrices. MUMPS is a multifrontal solver. It means that several frontal solvers are implemented on numerous indipendent fronts, which can work in parallel, even in different processors. Moreover, a frontal solver approaches the solution of sparse linear systems, characteristic of FEM, automatically avoiding zero terms.
Specifically, Newton highly nonlinear method has been adopted. The computation is stopped when a maximum number of iterations equal to 25 is reached without satisfying the tolerance requirements, hence when convergence criteria are not satisfied.

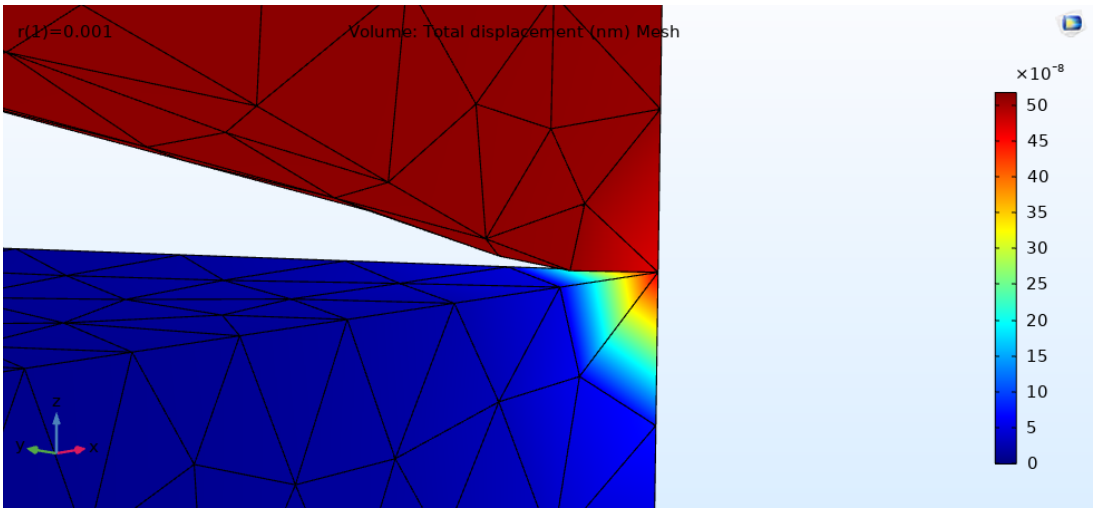

Figure 5.12: *Complete model with mesh at the beginning of test: onset of contact*

Results

6

6.1 | Experiment

6.1.1 | Nanoindentation

Top surface

Sample	Young Modulus [GPa]	Hardness [GPa]	Load [mN]
Heat treated	128	6.5	1
	106	7	5
	93	7.2	10
200μm	134	5.6	1
	131	6.4	5
	127	6.8	10
100μm	135	5.8	1
	129	6.3	5
	125	6.8	10
45μm	125	5.5	1
	118	5.9	5
	119	5.8	10

Table 6.1: Values of relative Young Modulus and hardness for three different peak loads and same loading rate 50$\mu N/s$ and hold time 30s, indentation performed on top surface

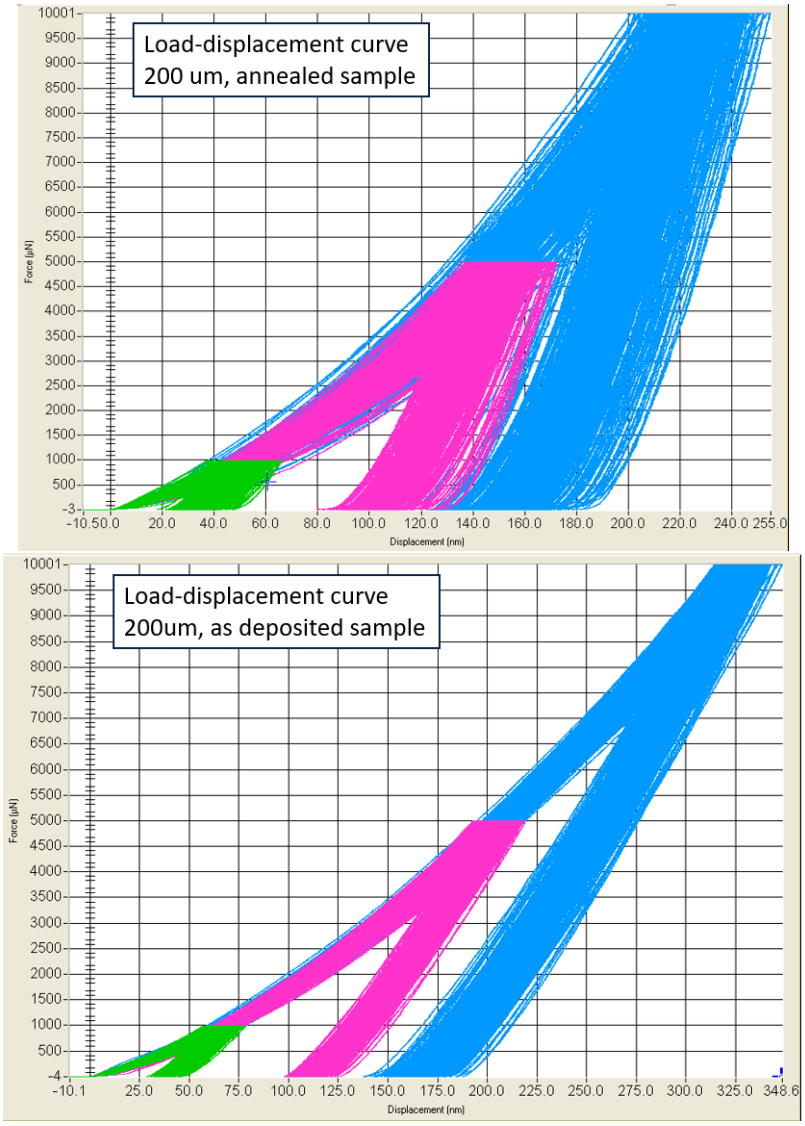

Figure 6.1: *Load-displacement curves of* $200\mu m$ *thickness samples: annealed and as deposited. Different peak loads, hold time* $30s$ *and loading rate* $50\mu N/s$.

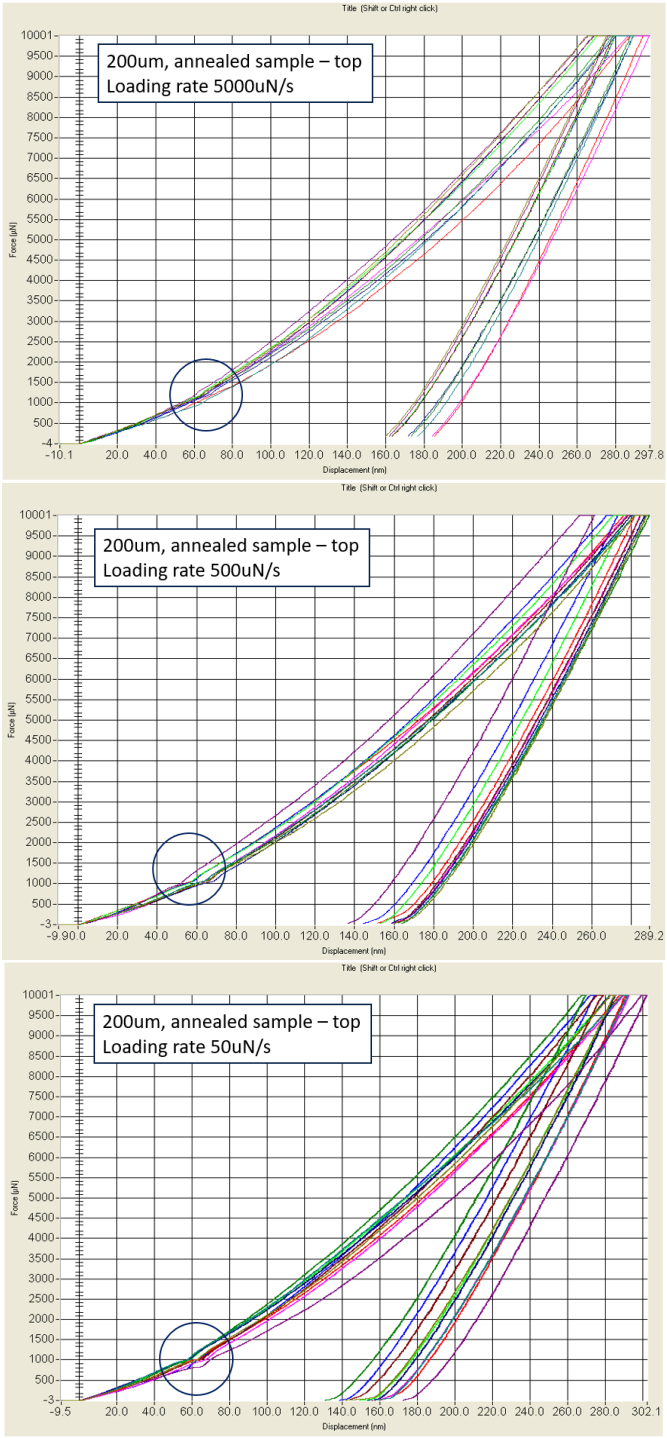

Figure 6.2: *Load-displacement curves of* 200μm *thickness, annealed sample. Peak load* 10mN*, hold time* 30s *and variable loading rate:* 5000$\mu N/s$*,* 500$\mu N/s$ *and* 50$\mu N/s$*.*

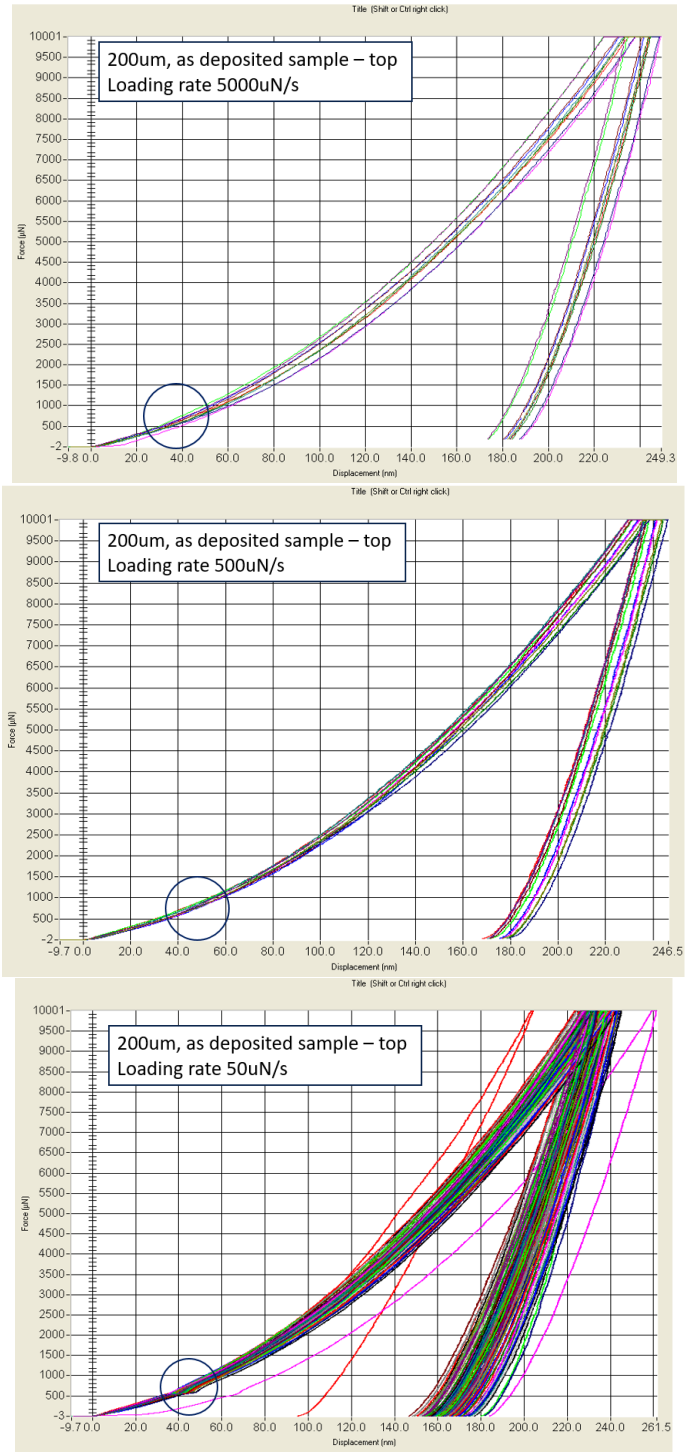

Figure 6.3: *Load-displacement curves of* $200\mu m$ *thickness, as deposited sample. Peak load* $10mN$*, hold time* $30s$ *and variable loading rate:* $5000\mu N/s$*,* $500\mu N/s$ *and* $50\mu N/s$*.*

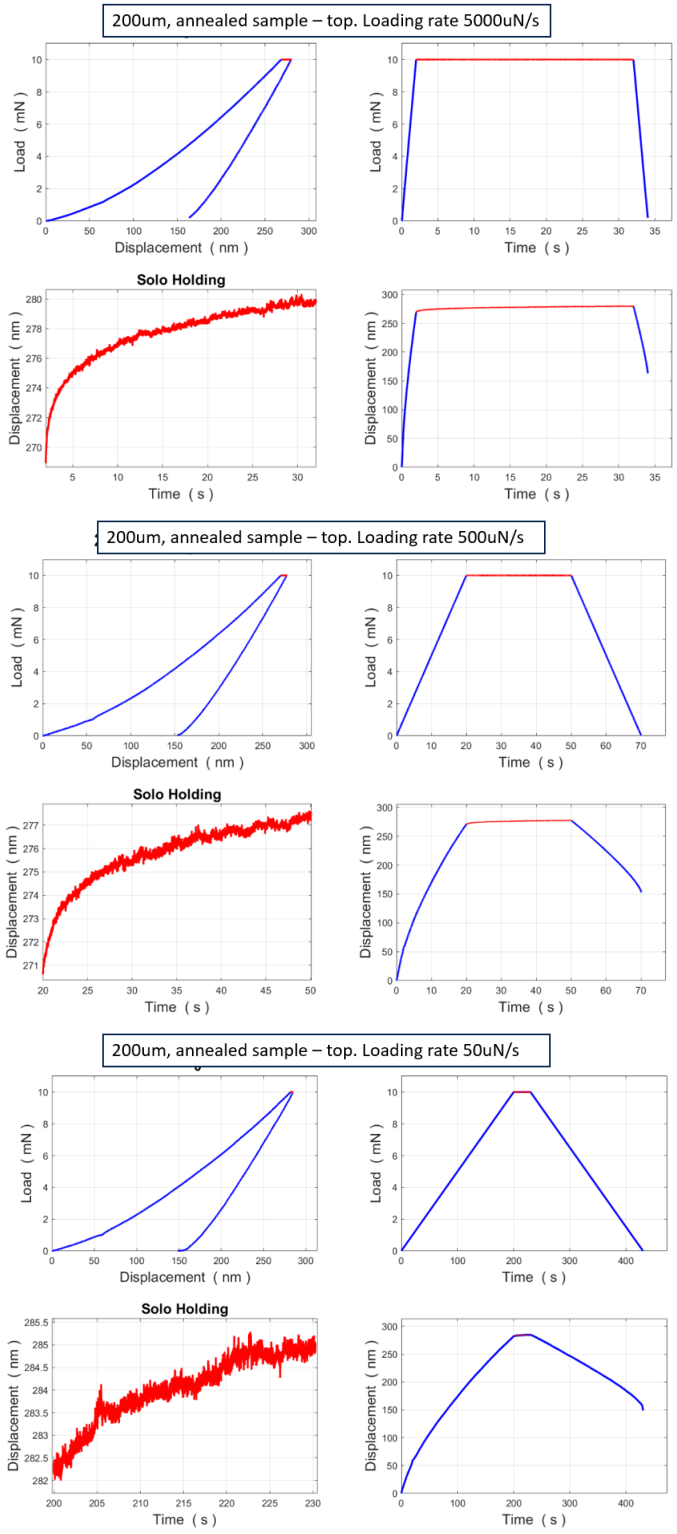

Figure 6.4: *Detail of curves of* 200μm *thickness, annealed sample.*

Cross section surface

Sample	Young Modulus [GPa]	Hardness [GPa]	Load [mN]
Heat treated	148	6.1	1
	158	6.8	5
	154	7	10
$200\mu m$	132	6	1
	126	6.3	5
	121	7	10
$100\mu m$	149	6.6	1
	139	7.4	5
	135	7.5	10

Table 6.2: Values of relative Young Modulus and hardness for three different peak loads and same loading rate $50\mu N/s$ and hold time 30s, indentation performed on cross section surface

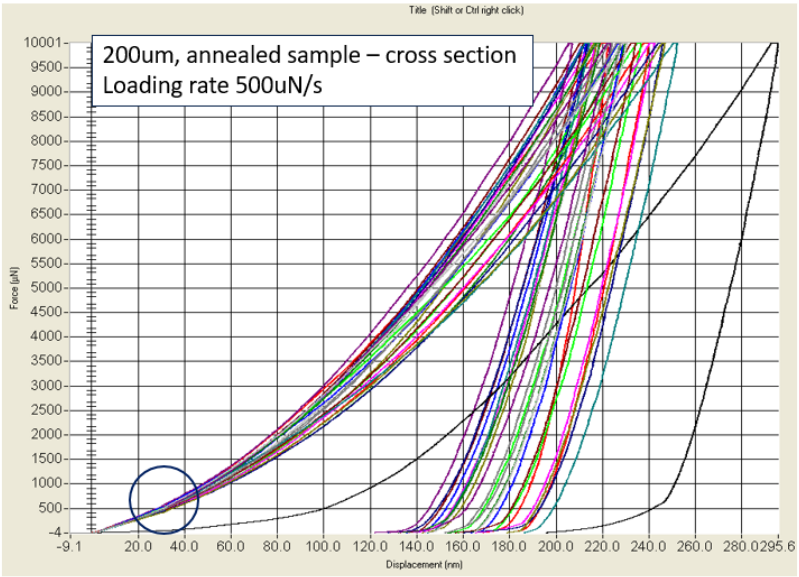

Figure 6.5: *Load-displacement curve of* $200\mu m$ *thickness, annealed cross section sample. Peak load* $10mN$*, hold time* 30s *and loading rate* $500\mu N/s$*.*

6.1.2 | SEM-TEM observation

SEM: comparison $200\mu m$ thickness sample as deposited and heat treated

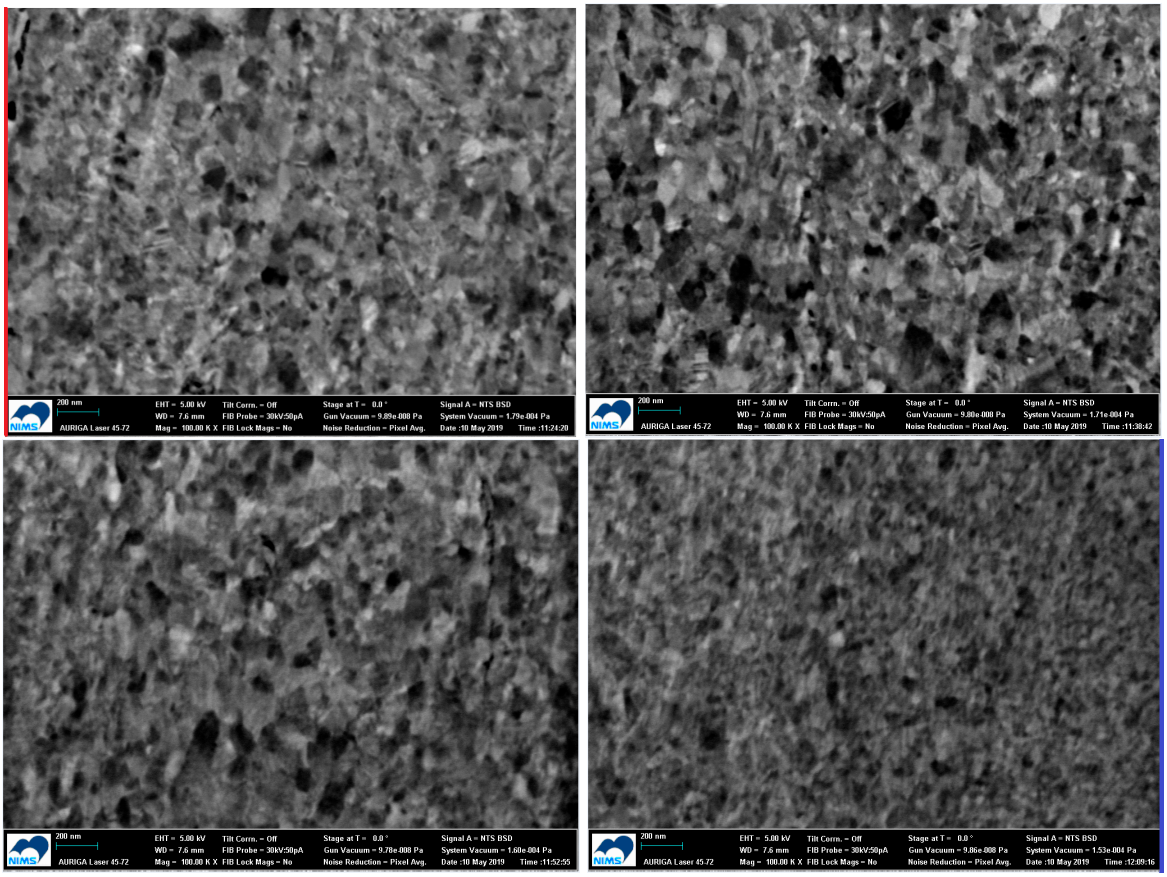

Figure 6.6: *SEM observation $200\mu m$ thickness, as deposited, cross section resin mounted specimen*

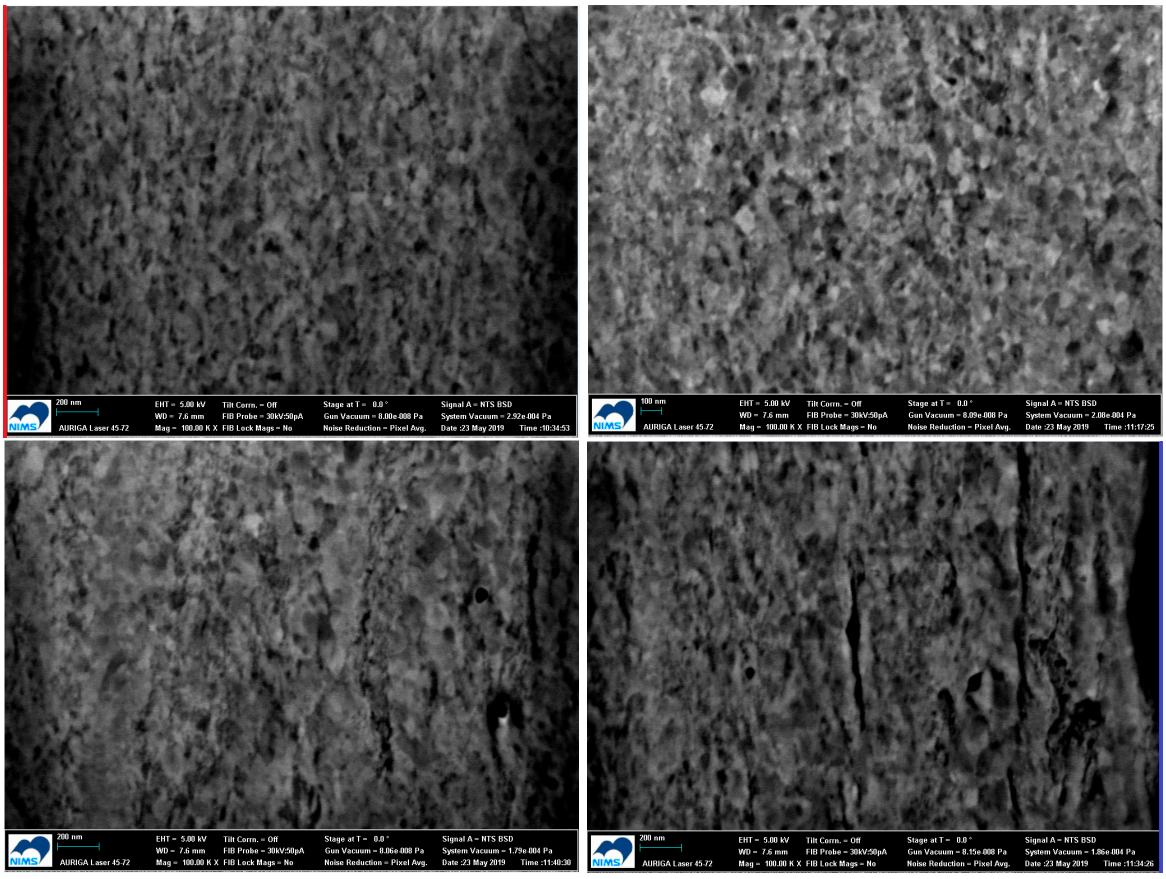

Figure 6.7: *SEM observation* 200μm *thickness, annealed at* 370°*C, cross section resin mounted specimen*

TEM: $200\mu m$ **and** $100\mu m$ **thickness sample as deposited, top surface and cross section lamellae**

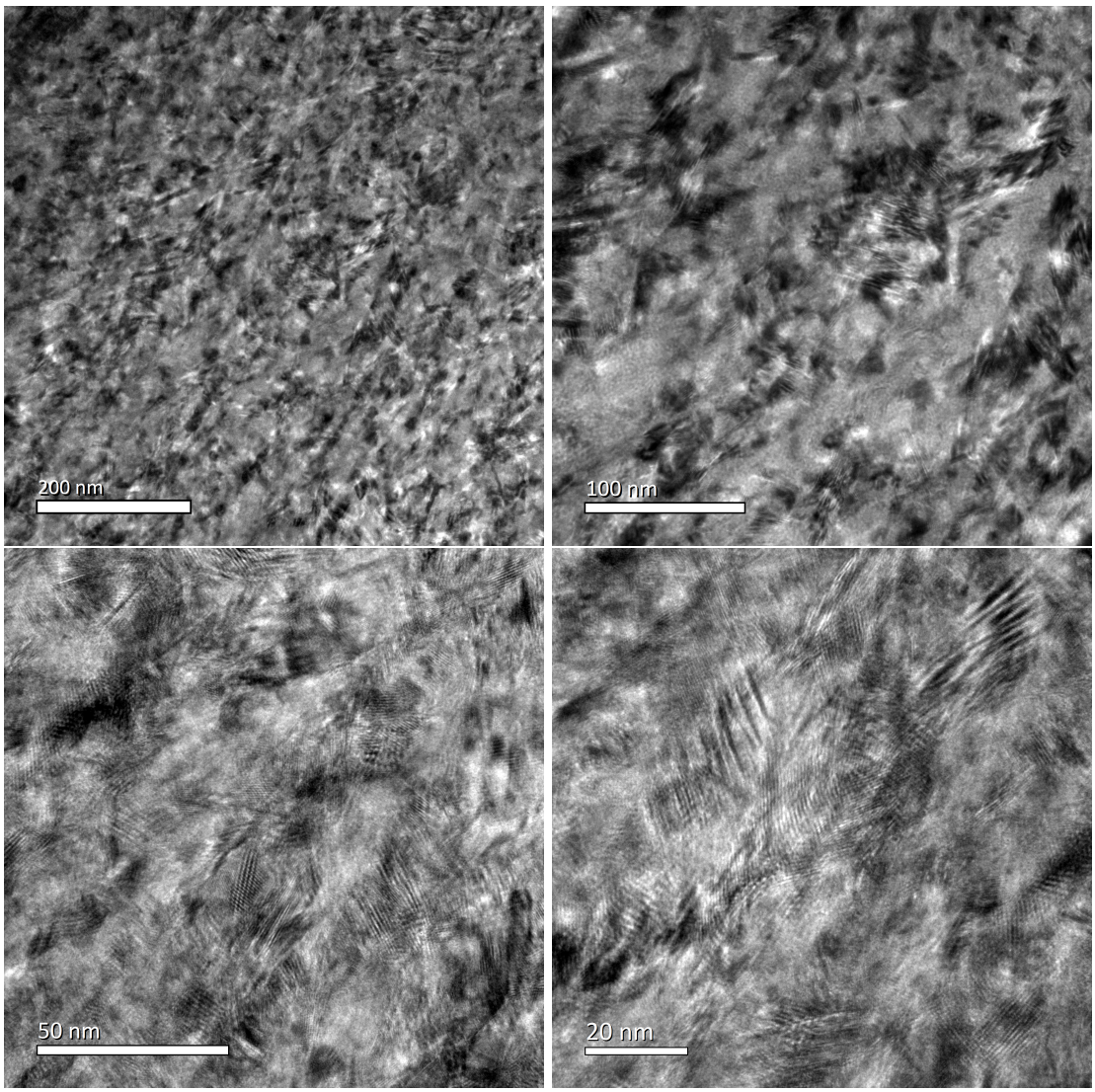

Figure 6.8: *TEM observation* $200\mu m$ *thickness, as deposited sample: top surface*

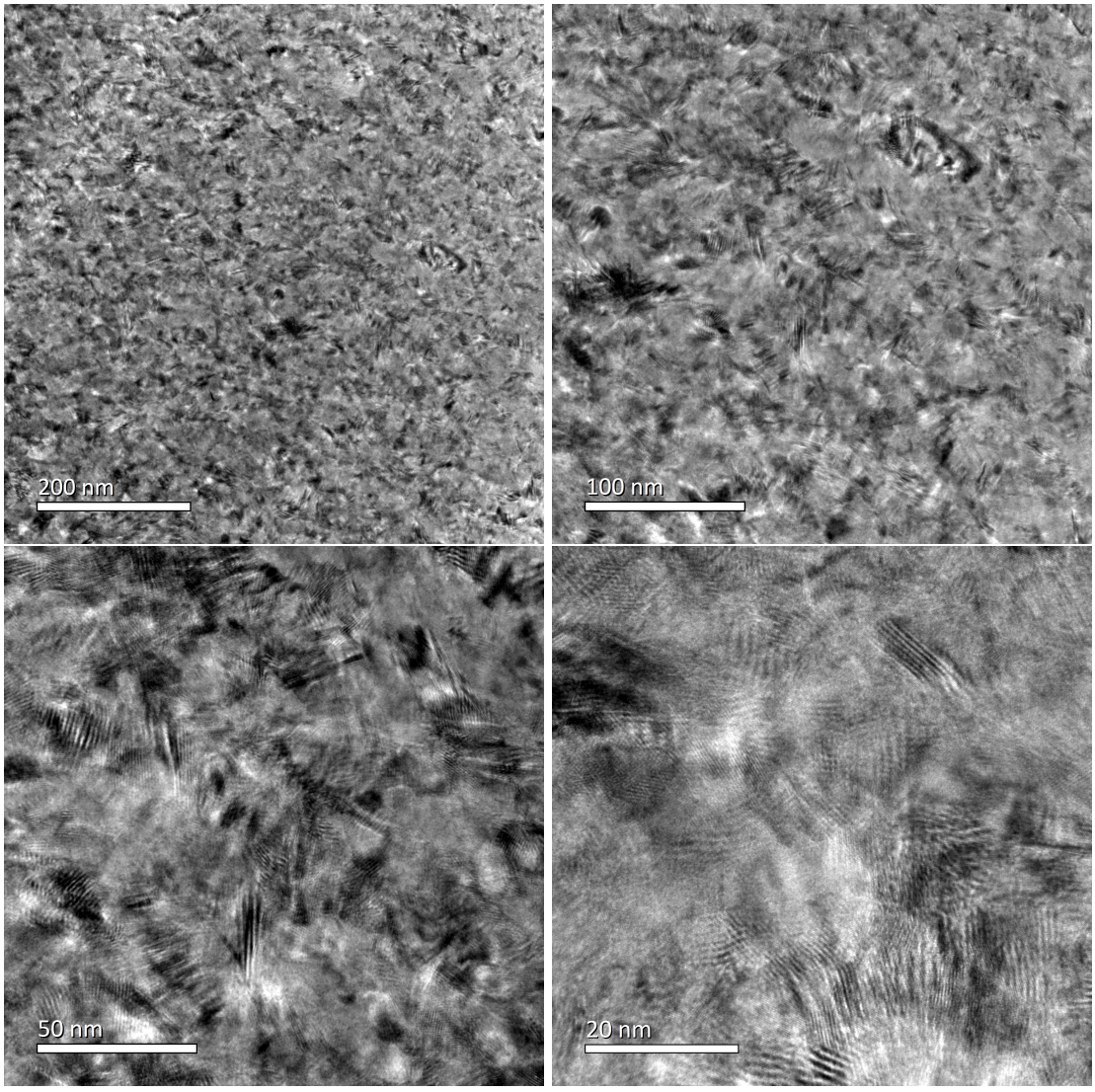

Figure 6.9: *TEM observation* 200μm *thickness, as deposited sample: cross section surface*

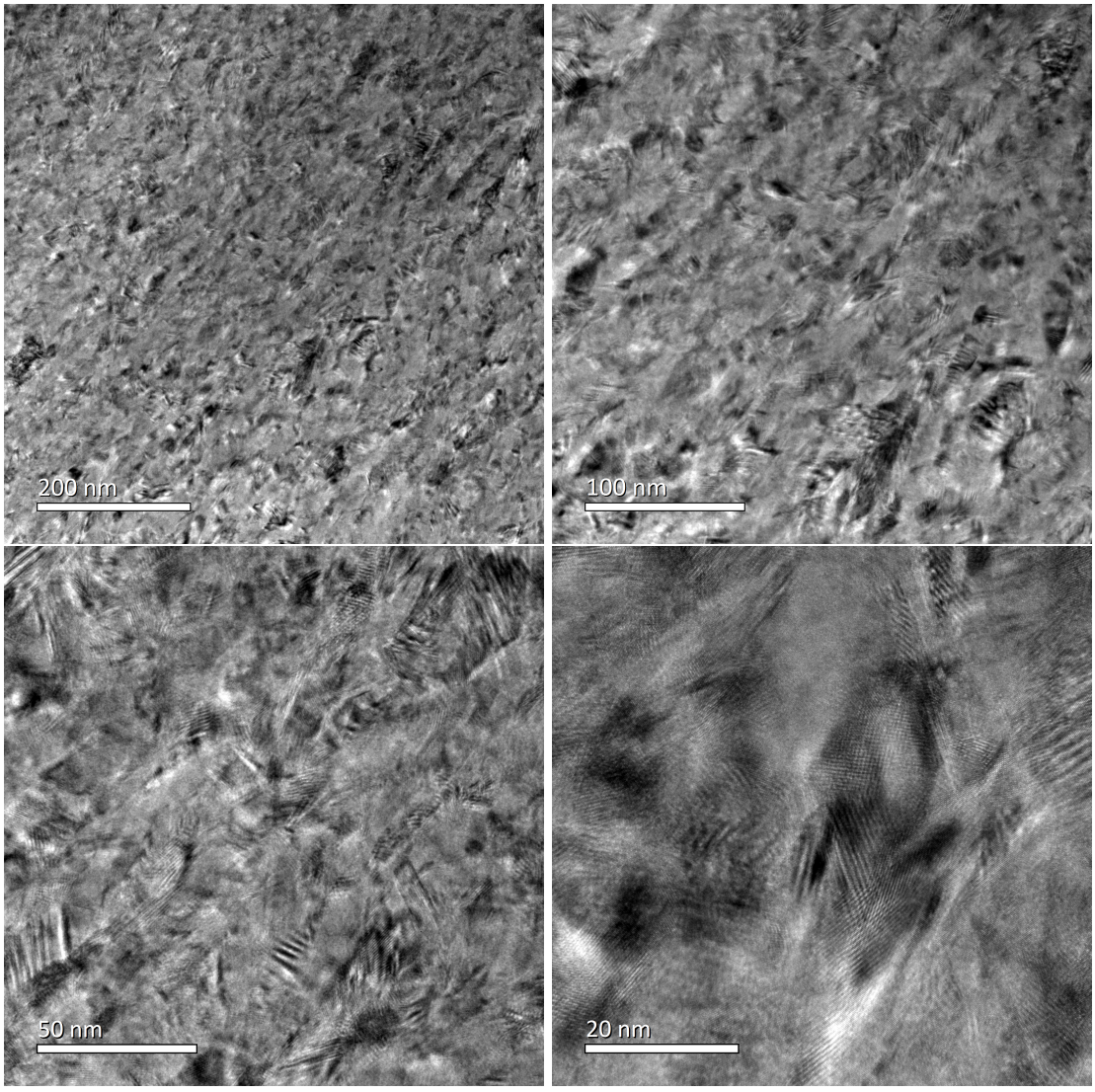

Figure 6.10: *TEM observation* 100*µm thickness, as deposited sample: top surface*

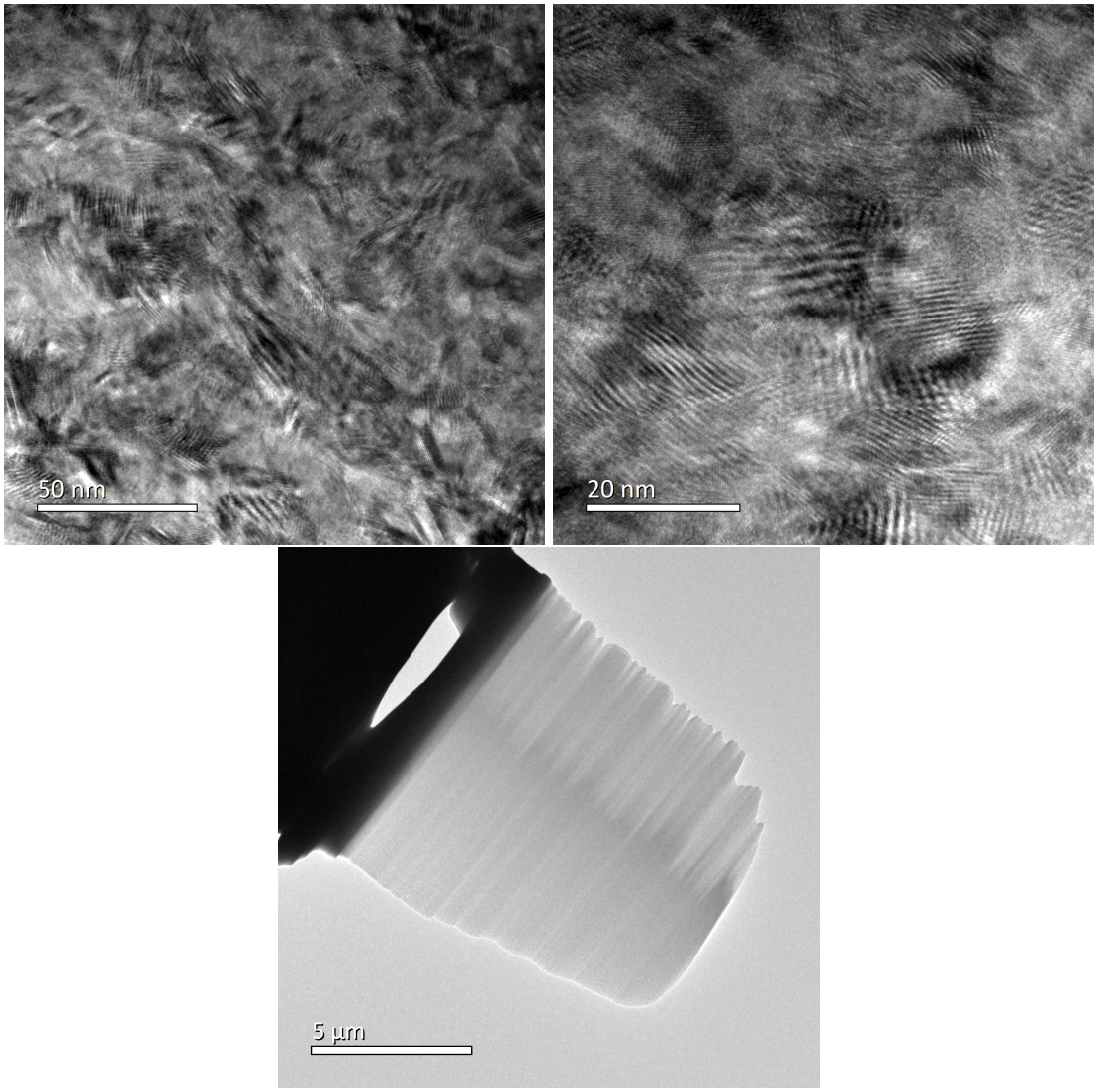

Figure 6.11: *TEM observation* 100*µm thickness, as deposited sample: cross section surface*

TEM: $200\mu m$ **thickness, as deposited, top surface sample with indentation mark**

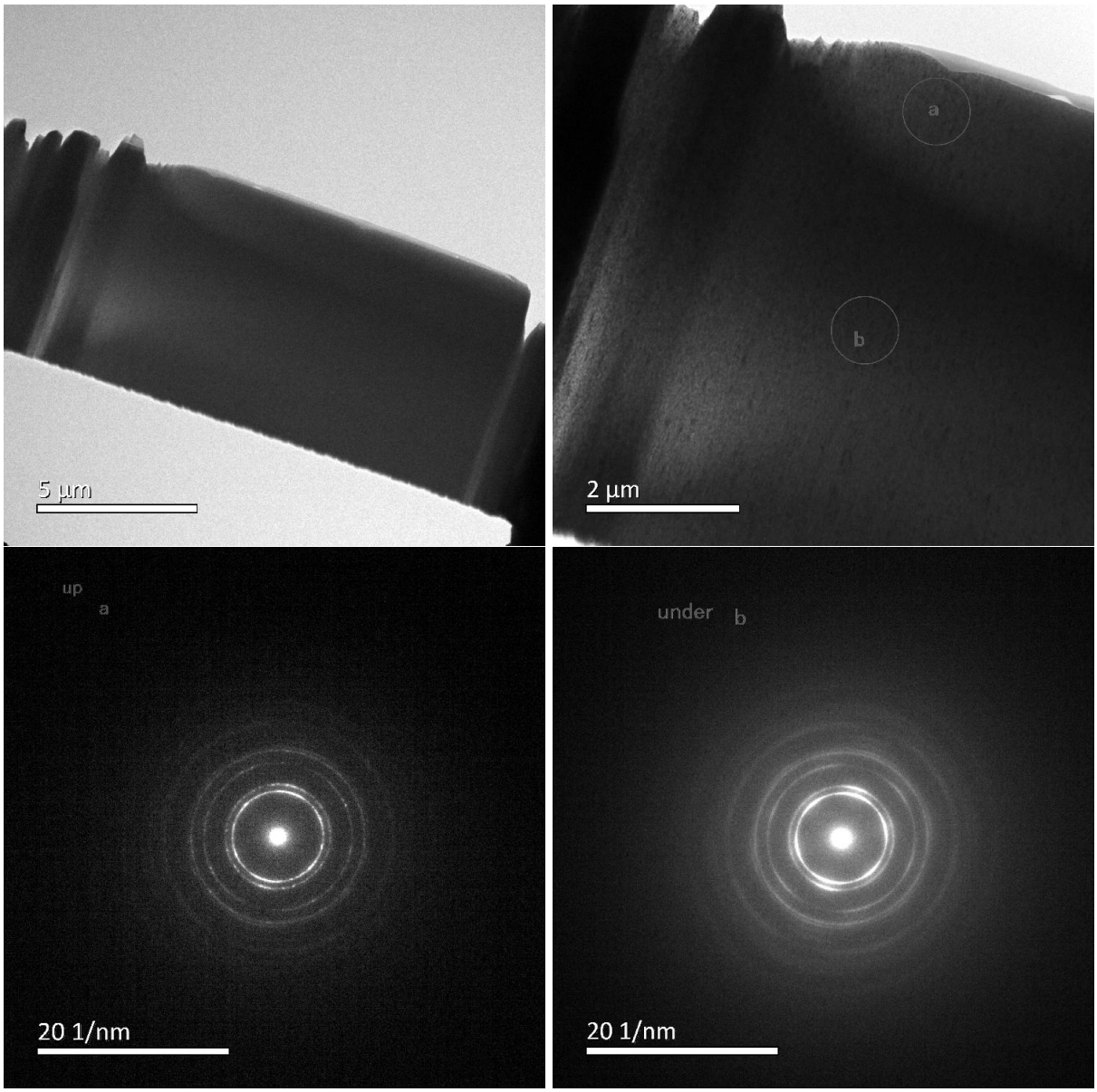

Figure 6.12: *TEM observation* $200\mu m$ *thickness, as deposited, top surface sample: lamella and diffraction patterns*

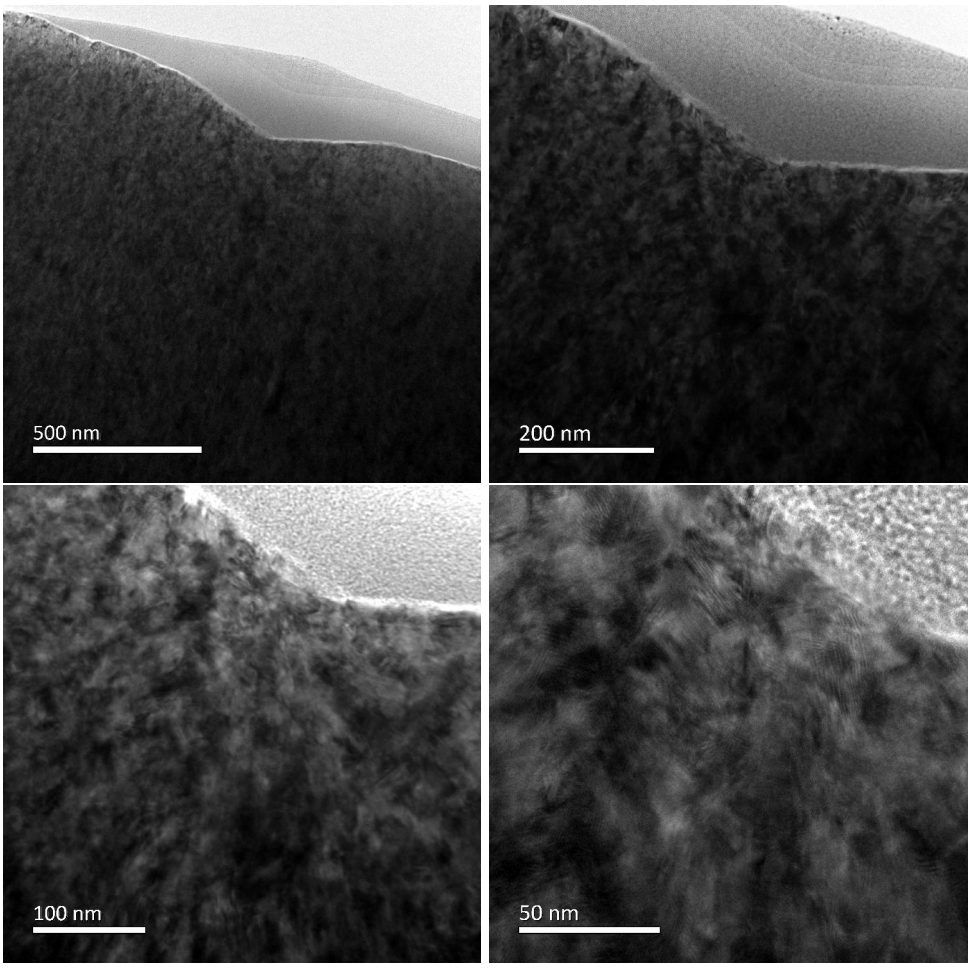

Figure 6.13: *TEM observation* 200*µm thickness, as deposited, top surface sample: magnification of under tip region*

6.1.3 | SEM- EDS

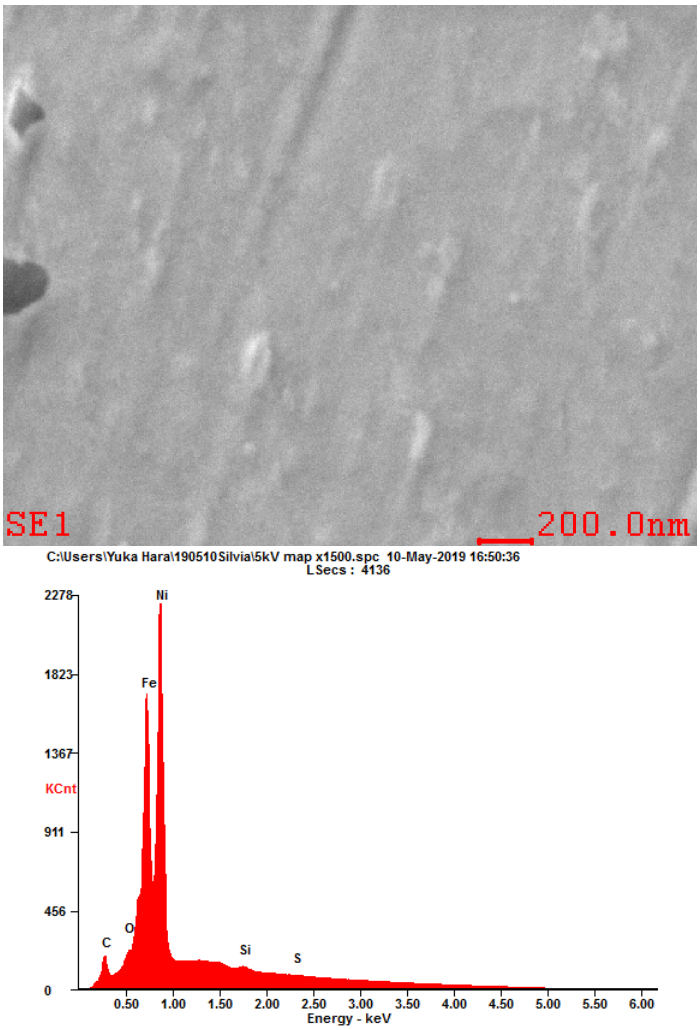

Figure 6.14: *Investigated region of Os coated* 200μm *thickness, as deposited, resin mounted cross section sample and spectrum*

EDS mapping has been conducted on a 200μm thickness, as deposited, Os coated, cross section resin mounted sample. Accelerating voltage was set to 5kV and the mapping run for 45 minutes. The investigated elements were: nikel, iron, oxygen, carbon, silica and sulfur. Drift was encountered at a minor extent, on the other hand damage to the sample had a considerable impact on the sample surface, as shown in figure 6.16 at page 64.

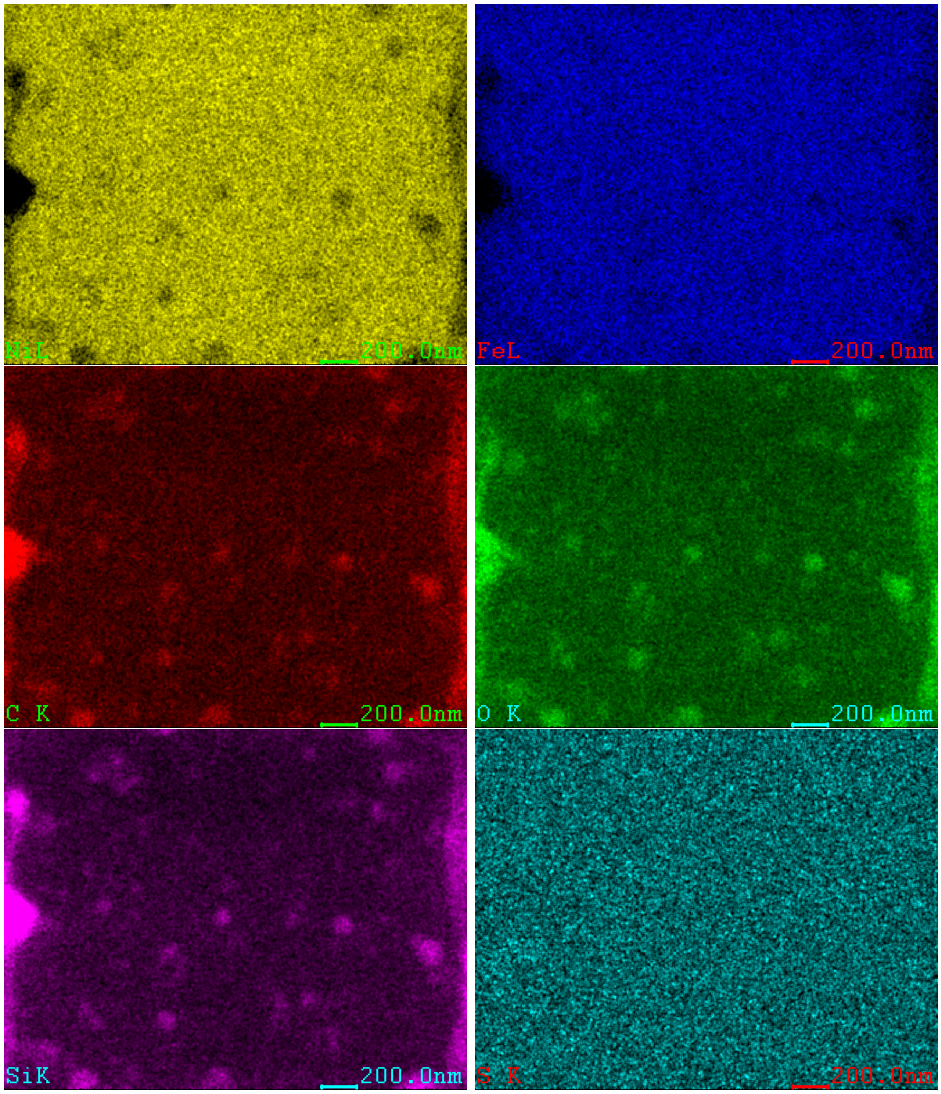

Figure 6.15: *SEM EDS map - EHT 5kV for elements: nikel, iron, oxygen, carbon, silica, sulfur*

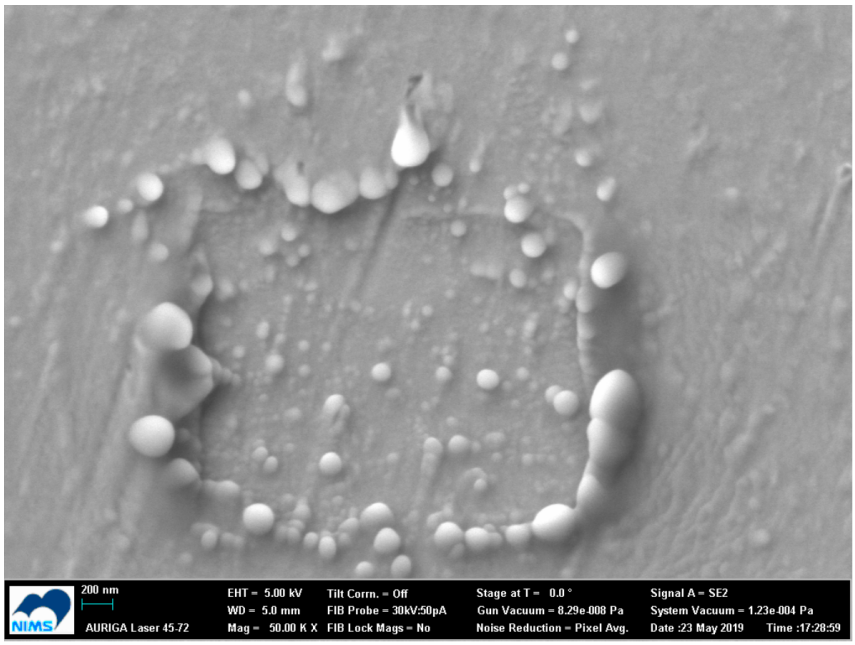

Figure 6.16: *Damaged surface*

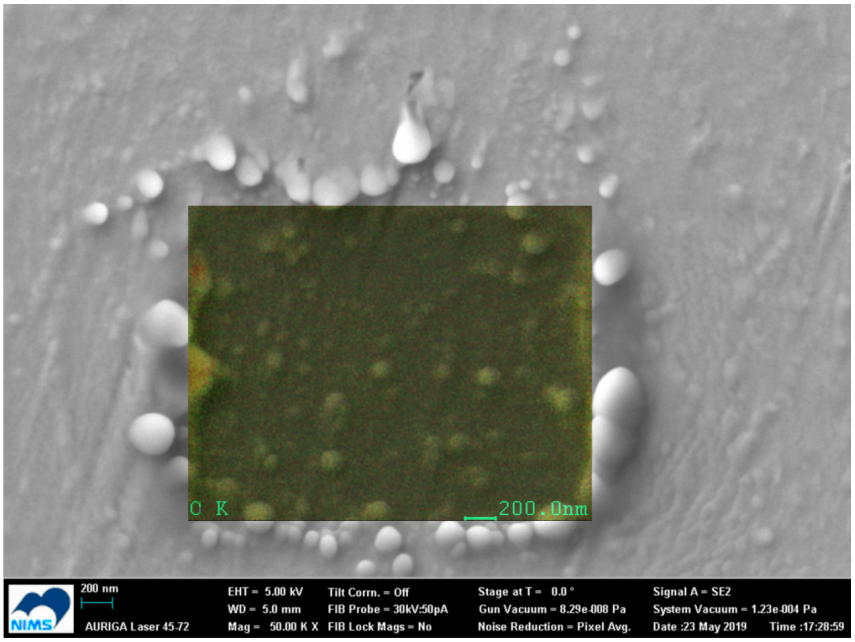

Figure 6.17: *Superimposition of damaged surface and EDS map*

6.1.4 | SEM -EBSD

EBSD analysis has been performed on 200μm thickness, as deposited, Os coated sample on two regions on the cross section surface, namely close to the top surface and in the middle part. Moreover, EBSD and EDS have been done simultaneously on a region close to top surface, with value of accelerating voltage equal to 15kV and stepsize 0.01μm, confidence index (CI) greater than 0.1.

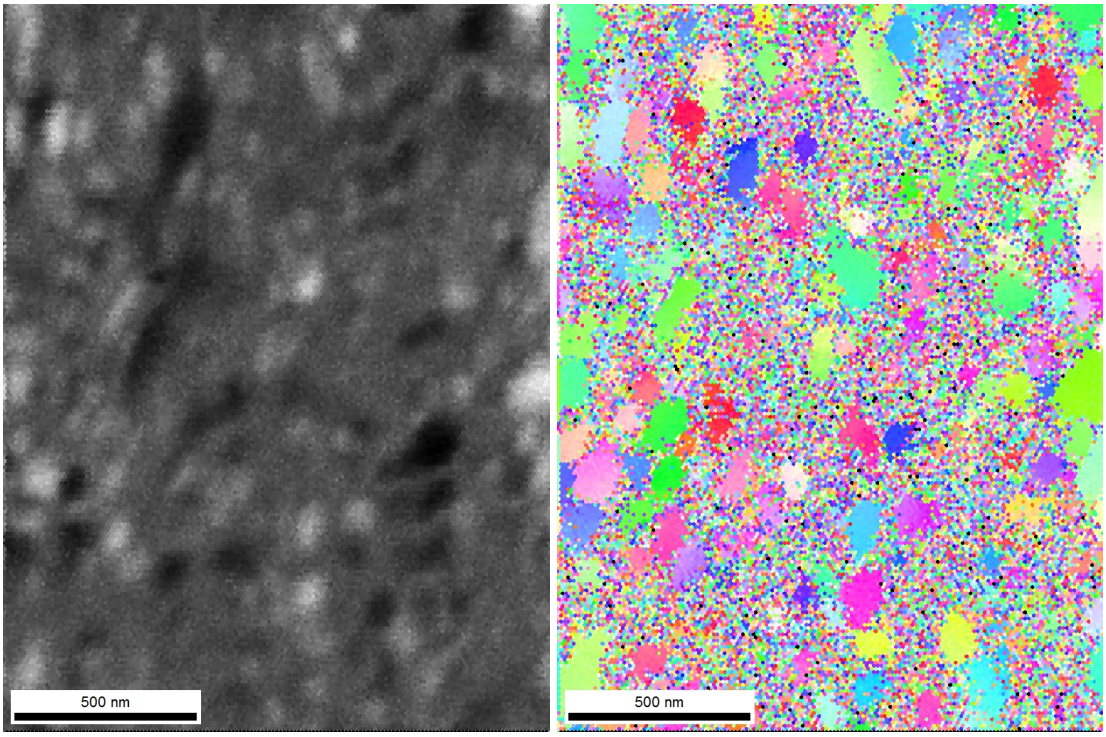

Figure 6.18: *Simultaneous EBSD-EDS: IQ (image quality) and IPF (inverse pole figure)*

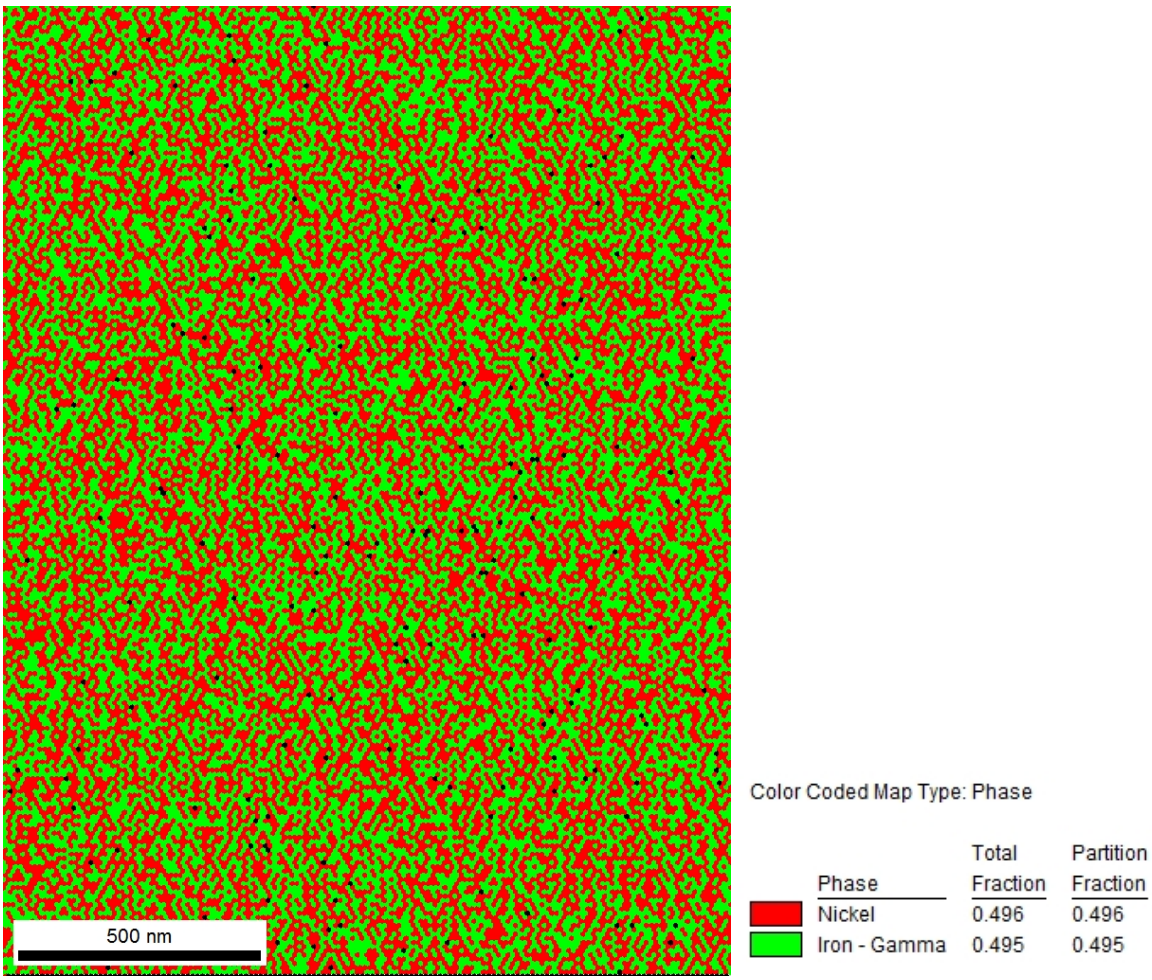

Figure 6.19: *Simultaneous EBSD-EDS: Ni and Fe distribution*

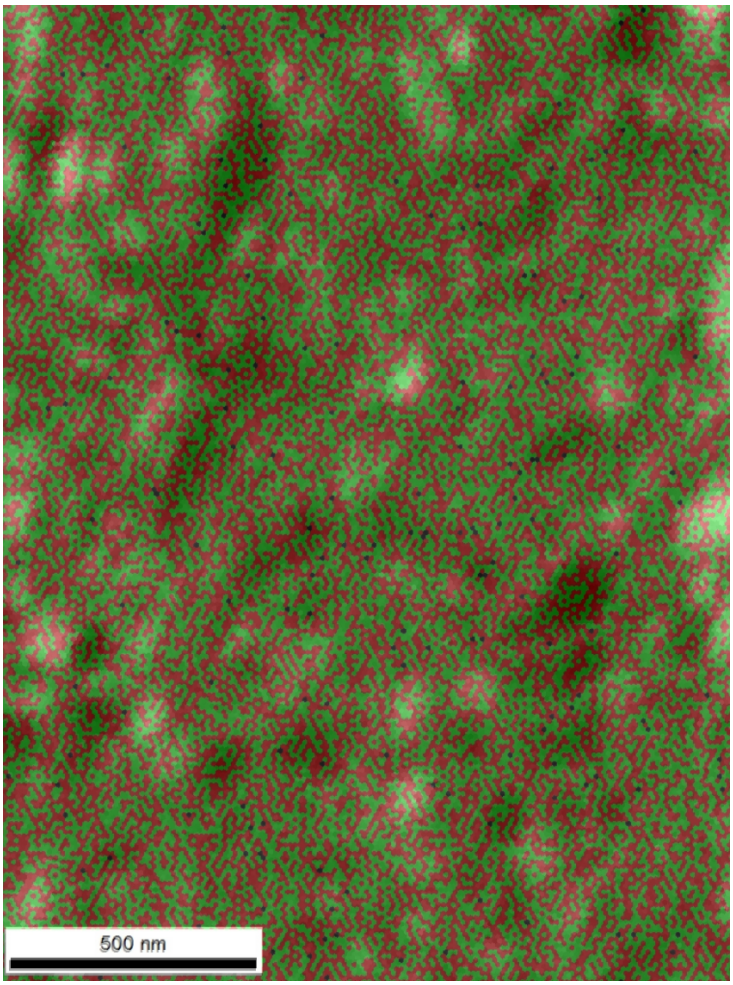

Figure 6.20: *Simultaneous EBSD-EDS: superimposition of IQ map and Ni-Fe distribution map*

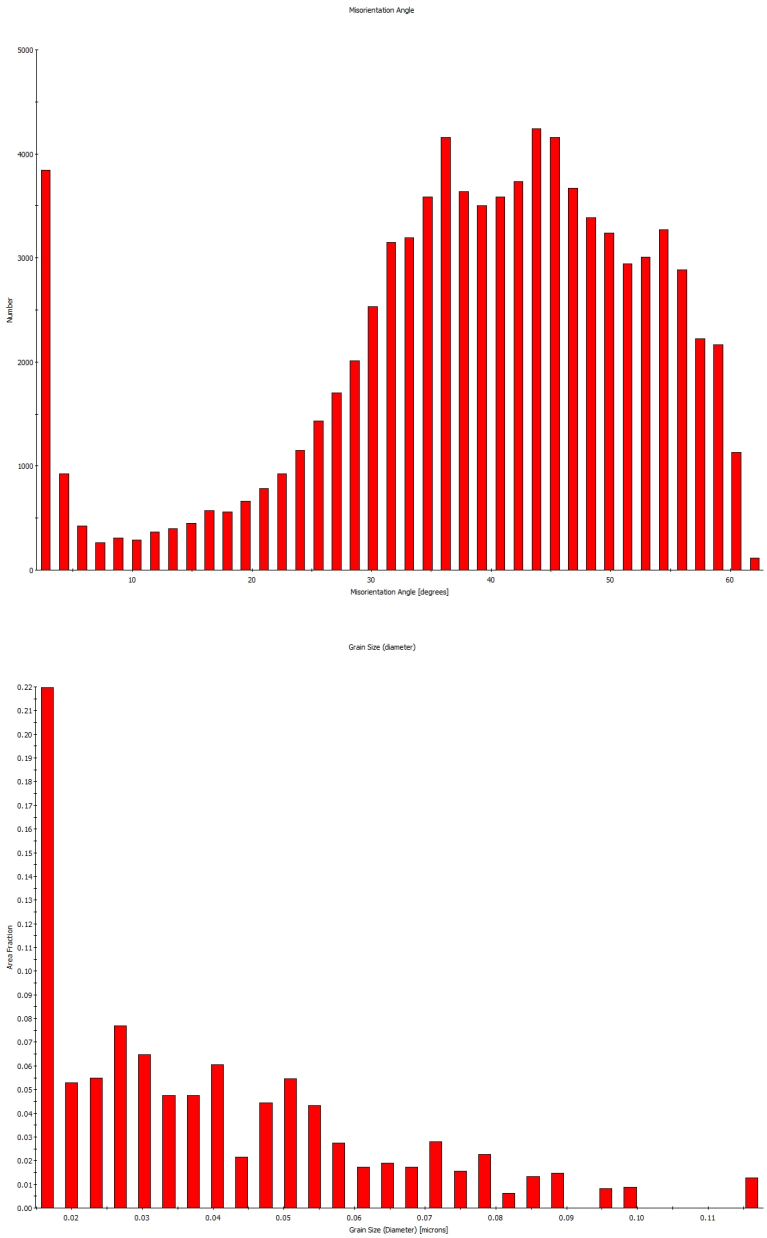

Figure 6.21: *Simultaneous EBSD-EDS: misorientation and grain size distribution*

6.1.5 | TEM -EDS

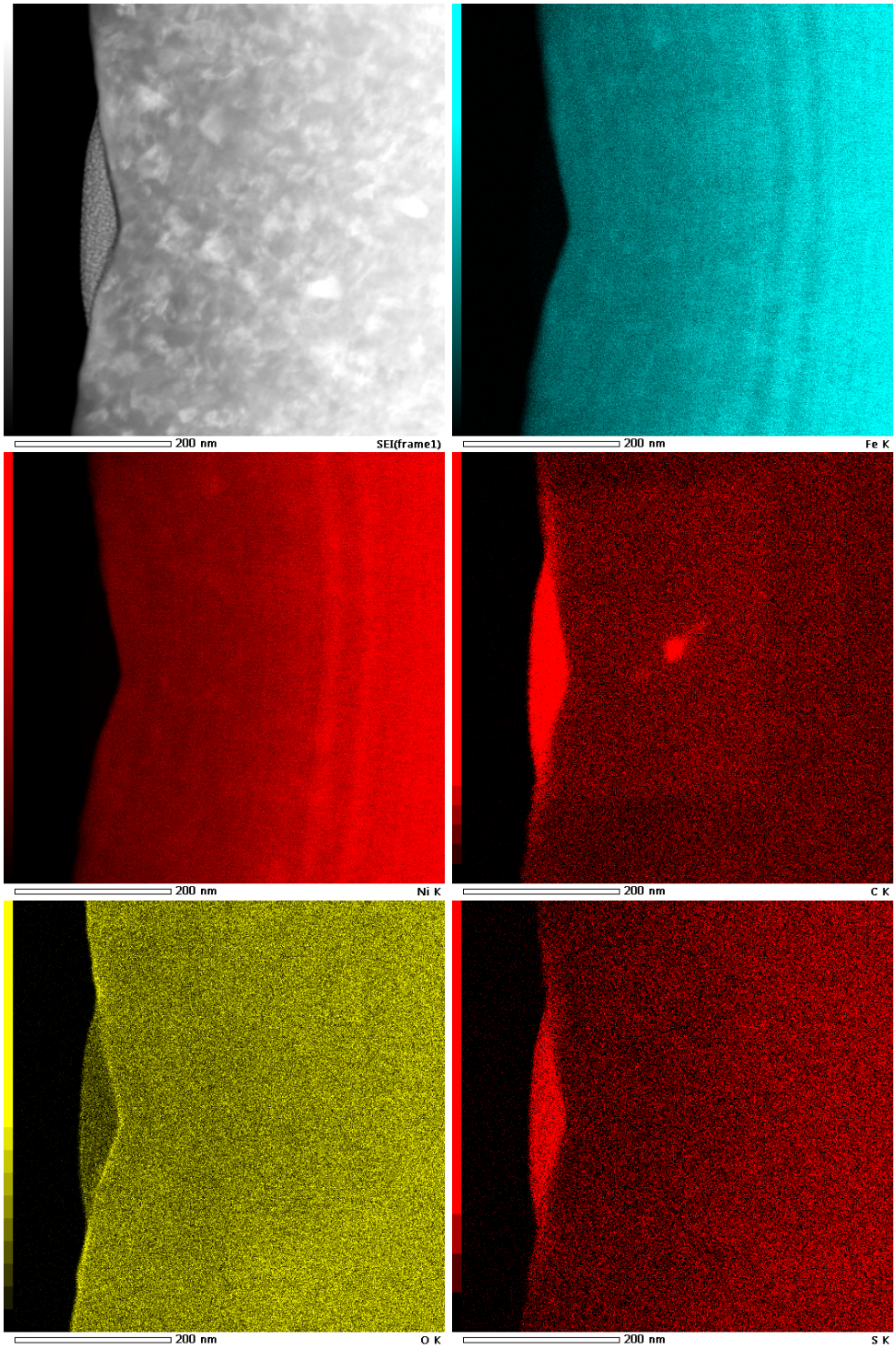

Figure 6.22: *TEM-EDS: region of interest with indentation mark and maps of iron, nickel, carbon, oxygen and sulfur*

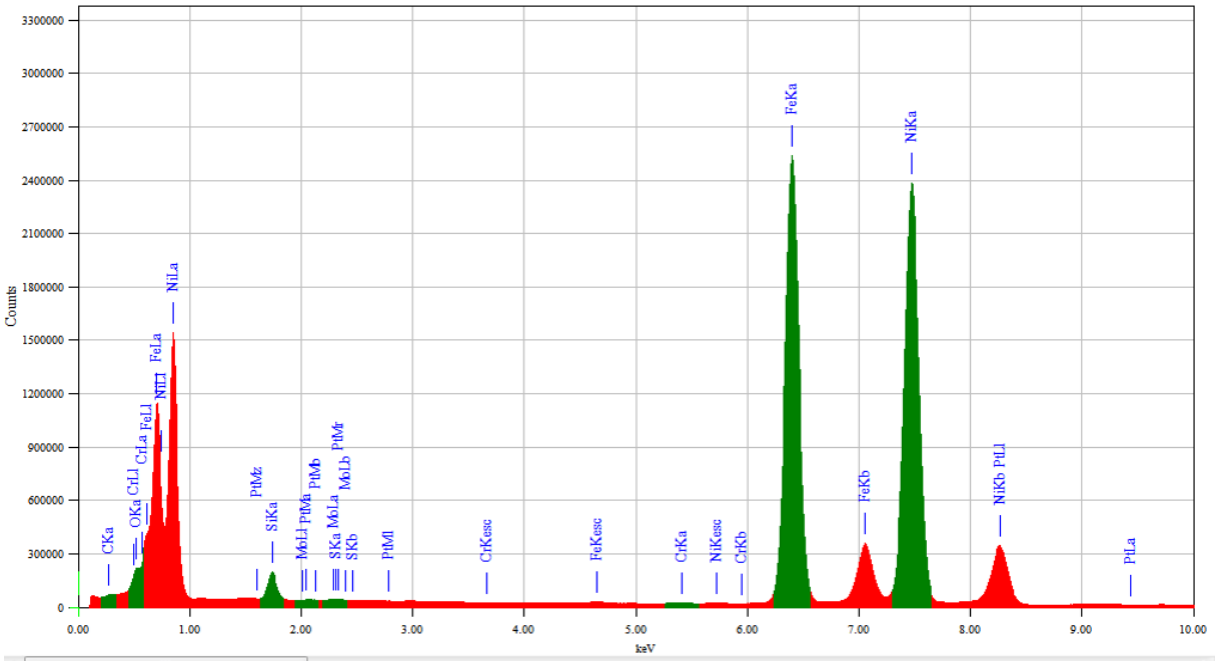

Figure 6.23: *Spectrum of EDS analysis performed with TEM*

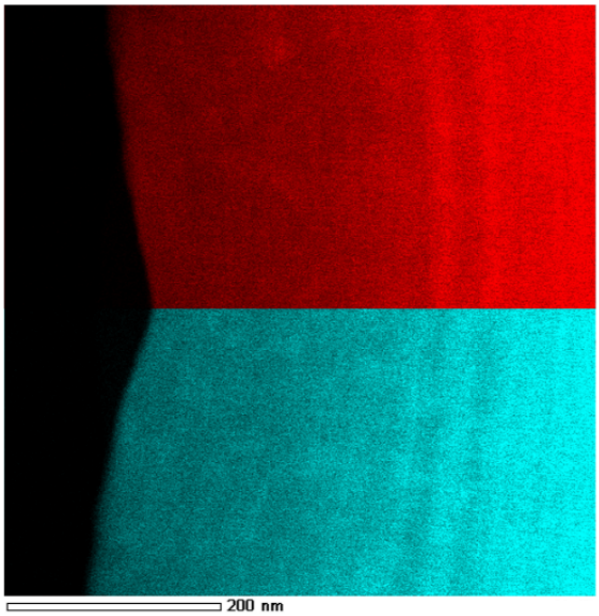

Figure 6.24: *Comparison of EDS maps of nickel and iron*

6.1.6 | TEM -EELS

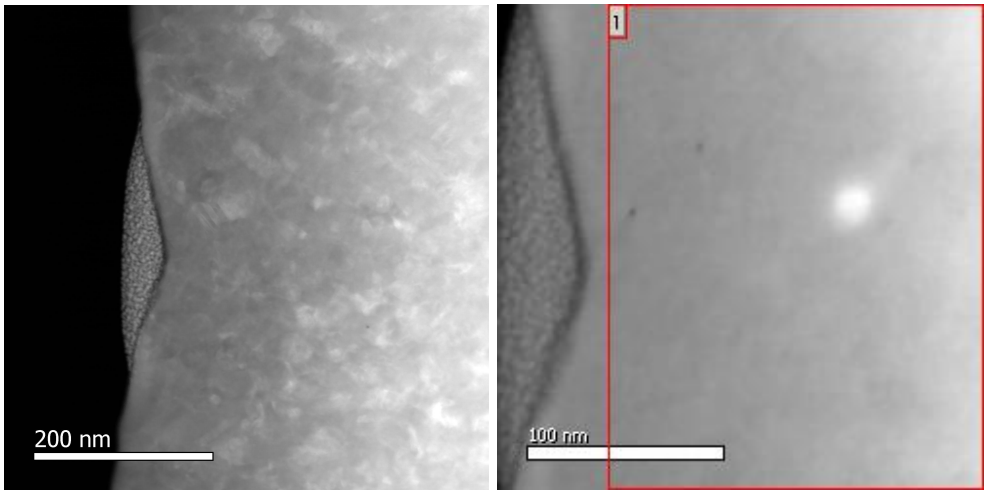

Figure 6.25: *Region of interest for EELS: under indentation mark*

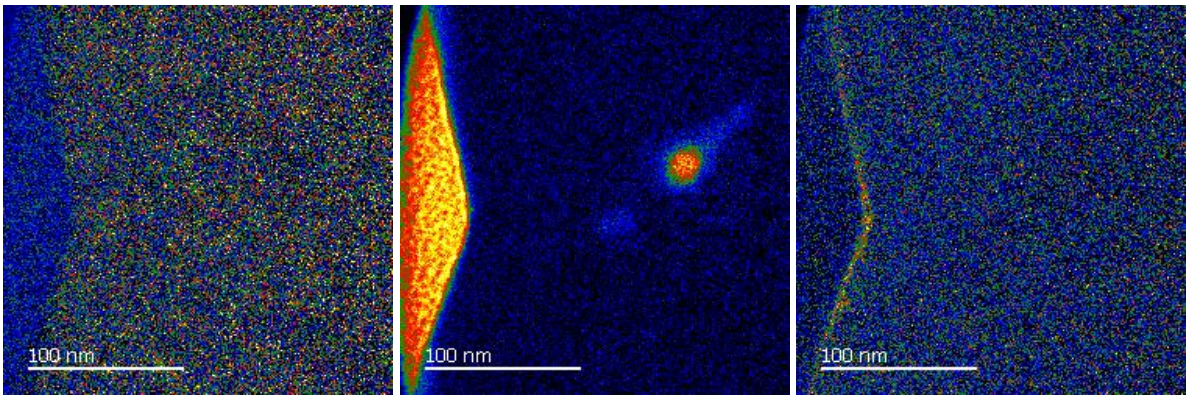

Figure 6.26: *EELS: pictures obtained in correspondance to different signal bands*
Sulfur: $162 - 182eV$
Carbon: $279.3 - 299.3eV$
Oxygen: $527.5 - 547.5eV$

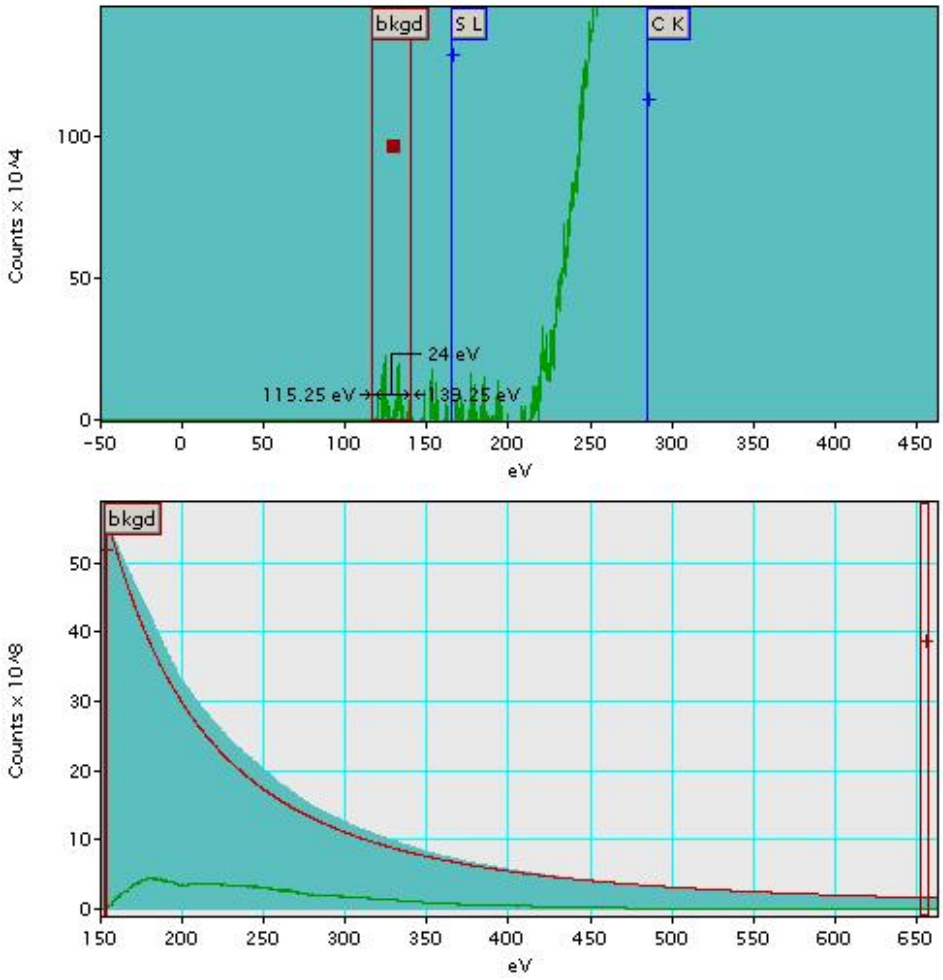

Figure 6.27: *EELS: spectrum*

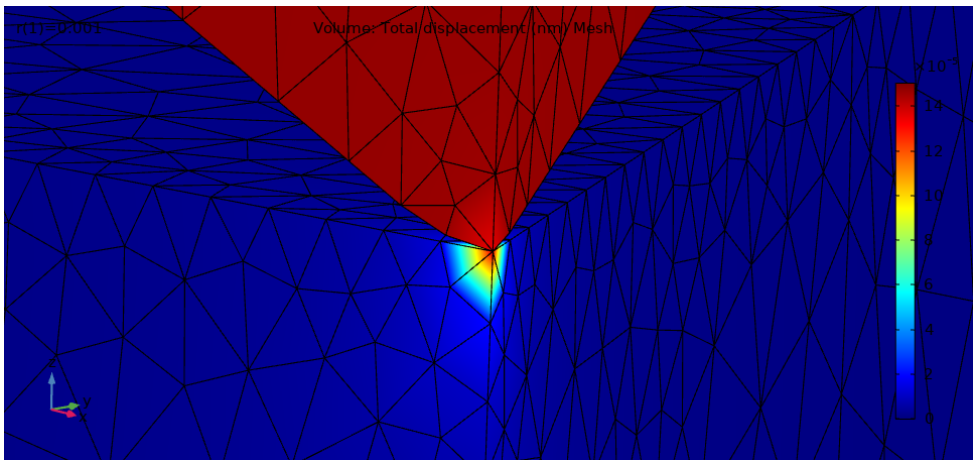

Figure 6.28: *One sixth of 3D model during test. Spherical color gradient at deformation.*

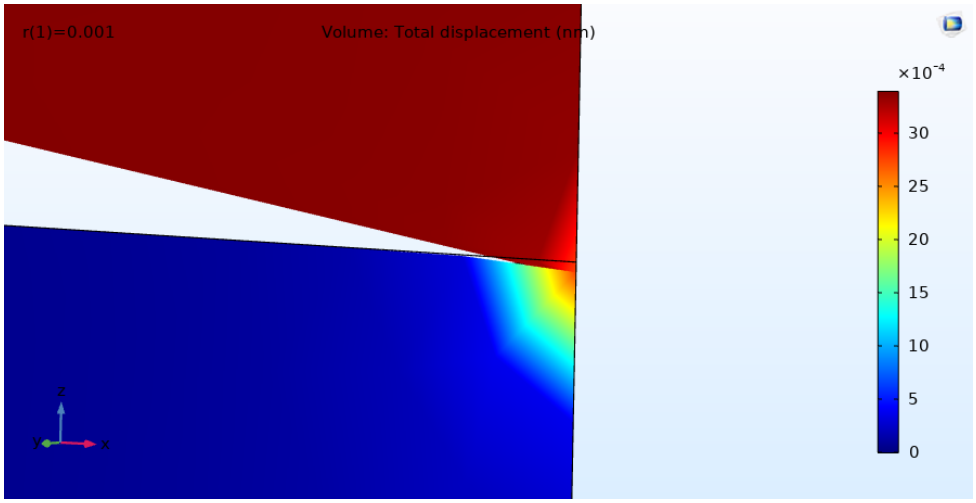

Figure 6.29: *Interaction between spherical tip of indenter and sample*

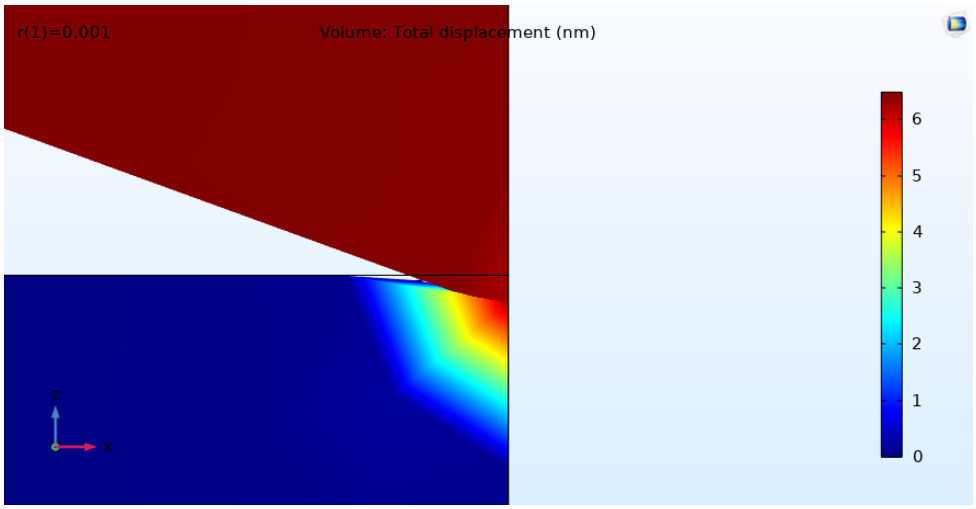

Figure 6.30: *View on plane xz of nanoindentation test: interaction spherical tip of indenter and sample*

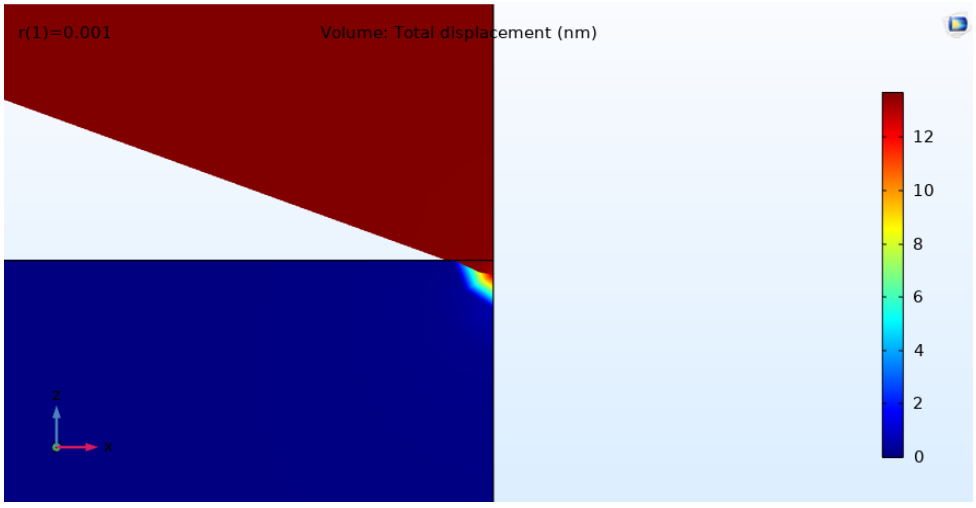

Figure 6.31: *View on plane xz of nanoindentation test: transition from spherical to planar indentation*

7 Discussion

Nanoindentation tests performed on top surface of the samples show a decrease of measured Young's modulus value and an increase in measured value of hardness when the peak load is increased, for the automatic loading rate set in the machine, namely $50\mu N/s$ as reported in table 6.1. Such behaviour can be verified on load-diaplacement curves in figure 6.1: curves are grouped for maximum peak load and the respective unloading segments have different angular coefficient. The hypothesis of an hardness gradient has been investigated with nanoindentation test on cross section surface. The same trends can be found for these tests as well, as shown in table 6.2. The values shown both in table 6.1 and 6.2 have been obtained performing 100 indentation tests on each sample for each value of peak load and post processed and filtered to eliminate tests affected by thermal drift error; tests have been considered representative for the population when the measured values fell in a range of $\pm$ one standard deviation. However, it it worth to underline that, in general, when considering a line of indentation tests performed from a region close to top surface to a region close to bottom surface, the values of Young modulus mesured close to the former are generally higher than the values measured thereby the latter. Such statement is true for a single line, it can not be applied to all lines together.

Three loading rates have been used for tests on both annealed and as deposited $200\mu m$ thickness sample to ivestigate the influence of loading rate and heat history on mechanical properties. In figure 6.2 and 6.3, load-displacement curves for both samples and different loading rates are reported. During the loading phase, a segment with different inclination has been encountered. This step follows the direction of the loading curve and it can be seen as the division of said curve in two parts. Moreover, the step is recorded at different loads in the two samples: it appears around higher loads in the annealed specimen. The hypotesis that can be made to explain the nature of this *step* is the possibility of a change of deformation mechanism, while the test is performed. Specifically, being the structure of the foil organised as a three levels hierarchy with columnar grains, characteristic grains and nano grains, deformation mechanism might involve nano grains at first and, from a certain moment on, larger grains. The known systems involved in this process are, respectively, grain boundary sliding and dislocation based mechanisms. Such hypotesis is reinfroced by

the fact that grain boundaries can be appreciated mainly in columnar grains, while nano grains are particularly hard to observe and distinguish from one another. Furthermore, the fact that the annealed sample is more compliant than the as deposited sample to the motion of the indenter can be a consequence of diffusivity processes which can occur during heat treatment.

The influence of loading rate on creep behaviour can be highlighted with relaxation curves, namaley time-displacement "solo holding" curves, in figure 6.4. While the curves plotted for a loading rate value equal to $5000\mu N/s$ and $500\mu N/s$ show a similar trend, the one obtainedd for $50\mu N/s$ does not respond to the same fitting. In fact, three segments with different inclination can be identified in the total hold time of $30s$: first $5s$, following $15s$ and final $10s$. Such differences can be ascribed to the events before the hold period, hence to the loading segment. Here the contributions to creep coming from the material and thermal effects could be playing different roles and contributing to different extents. For high loading rates, the plot can be fitted with an exponential function at first and then linearized, while for lower loading rates the plot can be immediately linearized, but it shows a different behaviour in the last $10s$. Hence, it is reasonable to think that when the peak load is reached in shorter time, so when the loading rate is high, thermal effects influence the test more and the curve that is recorded will show not only pure creep from the specimen, but also thermal creep. When the peak load is reached in a longer time, so when loading rate is low, thermal effects might still be present, but their contribution is expected to be reduced with respect to previous cases, for this reason exponential function does not represent a suitable fitting option.

To further investigate any peculiar characteristic of specimens along their thickness, both annealed and as deposited $200\mu m$ thickness samples have been observed with SEM. As shown in figure 6.7 and 6.6, bigger grains can be observed close to top surface, while smaller grains lay closer to the bottom surface. Moreover, from the comparison between the region close to top surface in both as deposited and annealed sample, it results that the sample which did not undergo heat treatment shows a bigger grain size on average. This could explain why during nanoindentation test performed on top surface (fig. 6.2 and 6.3), the transition from GBS to deformation due to dislocations happens at higher loads for the annealed sample. A smaller grain size can be seen as a bigger interface area between nano grains, hence more possibility to adjust to the indenter by grain boundary sliding. Furthermore, GBS is a fast deformation mechanism, which allows a fast response to the applied load, and it can explain why measured Young modulus values for annealed sample are smaller than the ones measured for as deposited sample, as reported in table 6.1. Furthermore, heat treament induces diffusivity in the material, hence energy coming from distrortion of the lattice is lower and measured Young's modulus values are, as well, lower than in as deposited sample. Moreover, nanoindentation tests performed on cross section of said samples show that Young's modulus values measured close to top surface

are in general higher than the ones measured close to bottom surface and so, also this result, can be explained by the previous reasoning on SEM observation of cross section regions.

Lamellae from both $100\mu m$ and $200\mu m$ thickness samples, top and cross section, have been investigated with TEM to identify the presence of twin and tilt boundaries. Results are shown for top surfaces in figure 6.8 and 6.10 and for cross section in figure 6.9 and 6.11. Due to the extremely fine structure of the foil, it was not possible at this stage to clearly point out the presence of tilt and twin grain boundaries, but the investigation has proven useful in measuring grain size of the smallest grains. The higher magnification images have been used and a grain has been identified as a sequence of parallel lines. As regards this investigation such distance ranges between $4nm$ and $15nm$. No difference linkable to specimen thickness or region of extraction of the lamella has been found. Deformation area under indentation mark has been studied in the same way, as shown in figure 6.13, where the upper triangular region represents the platinum deposited to protect the sample during FIB preparation. The region of interest is the darker one, in which a certain deformation contour was expected to be observed. Both lower and higher magnification images do not give outstanding information about grain deformation and how the material adjusted to plastic deformation. However, two regions of the sample have been investigated in terms of diffraction patterns, namely one close to the tip of the indentation mark and one far from indentation surface. Obtained patters with respect to areas of interest can be seen in figure 6.12. The diffraction patterns obtained are rings, which means that the observed parts are polycristalline, FCC structure, as explained in chapter 4.1.2, and coherent with previous studies on similar samples, namely electrodeposited nanocrystalline Ni film with saccharine as additive in electrochemical bath [23].

The behaviour of the material can be strongly influenced by the presence of impurities and inclusions, other than nickel and iron. EDS analysis carried out on $200\mu m$ thickness as deposited, osmium coated sample studied the presence of nickel, iron, carbon, oxygen, sulfur and silicon, as shown in figure 6.14. The maps are showed in figure 6.15 and they portray a fairly homogeneous distribution of nickel and iron, while maps regarding carbon, oxygen and silicon do present some more intense spots. Specifically, on the left side of the frame, a silicon inclusion, probably due to polishing with colloidal silica of the sample, can be detected. Sulfur investigation results in a very homogeneous map, which does not give much information about the real presence of the element in the sample. However, severe damage was registered on the investigated region at the end of mapping process, as shown in figure 6.16. It is possible to link the damaged area to the working region of the electron beam used for EDS mapping. By superimposing maps and figure 6.16, it is possible to observe, in figure 6.17, that the dots recorded by oxygen, caarbon and silicon maps are due to the interaction with the sample. Actually, EDS mapping attempts have been performed also on sample which did not undergo osmium coating, but due to the high drift they

showed a proper mapping could only be obtained with a coating. Such coating did not prove to lead to reliable results for this material.

Distribution of nickel, iron and other elements on a larger scale has been studied with EBSD analysis, as shown in figure 6.18. Image quality gives a snapshot of the investigated area, while inverse pole figure provides information about orientation in the same way already presented in figure 4.16. Both nickel and iron present an FCC structure, hence the instrument did encounter some difficulties in discerning one from the other. In the end the map shown in figure 6.19 is obtained. It is interesting to notice that there are some black dots. It means that at in correspondance to those pixels the instrument did not detect either nickel or iron. If a superimposition of the latter map and the quality image is performed, as in figure 6.20, it can be noticed that the black dots lay in the dark regions of the QI. Considering the scale of the investigated area and misorientation and grain size distribution charts (fig. 6.21), it can be said that in the observed region different columnar grains can be found and the darker regions do represent grain boundaries. Misorientation angle distribution gives a relevant support to this idea because the highest number of encountered misorientation angles in the studied region is higher than 15°. Moreover, most of the analysed grains are nano grains, as confirmed by grain size distribution chart, which form characteristic grains in the QI picture, and they do have a similar orientation, leding to the only possible explanation for such an important number of high misorientation angles: columnar grains are being observed with their grain boundaries. It is at grain boundaries that most impurities can be found, as the map 6.19 suggested. Said grain boundaries are the ones to which the transition from GBS to deformation due to dislocation can be ascribed. In fact, load-displacement curves obtained with nanoindentation test on cross section (fig. 6.5) and curves obtained from the same test performed on top surface (fig. 6.2) of the annealed sample can be compared. Specifically, it can be noticed that the transition step appears at higher loads when the test is carried out on top surface, rather than cross section surface.

This behaviour can be explained by the composition of grain boundaries of columnar grains and by their shape, which has a dominant direction. Columnar grains grow perpendicularly to top surface and, hence, their characteristic direction is parallel to cross section surface. To ease the explanation, ordinary everyday objects such as strwas can be compared to columnar grains. The boarder of the straw is the grain boundary made of impurities and different elements, while the air contained in a straw is the nickel-iron structure with minor impurities. The sample is like a vertical rectangular parallelepiped box filled with straws in which the top surface is made of an ensamble of circles close to one another, while the side, hence the cross section, is an ensamble of long tubes. When the test is perfomed with the same loading rate on both top surface and cross section, the indenter will encounter grain boundaries of columnar grains at lower loads on the cross section rather than on top surface. The straw similarity is useful to understand that if an indenter starts the interaction

with the sample inside one of the circles, the adjustment will be very easy, hence the straws boardes will start to deform only after some time, when the indenter will touch them. While, if the same experiment is performed on the side of the box, the deformation will start in shorter time because the indenter will be more likely to be in contact with boardes of tubes, boundaries of columnar grains. Such behaviour can be experimentally encountered in the transition step that appears around $500\mu N$ for the cross section annealed sample and around $1000\mu N$ for top surface annealed sample. Before this transition, the material can rely on grain boundary sliding to adjust to the imposed load. Another way to see the phenomena is that when tests are perfomed on cross section surface, nano grains have less vertical room to move accordingly to the discending indenter, hence dislocations at grain boundaries have to comply to deformation starting at lower loads, hence lower indentation depths.

The spectrum shown in figure 6.23 refers to a further investigation on nickel, iron, oxygen, carbon and sulfur distribution with TEM. From the spectrum it is possible to see that also silicon, molybdenum and platinum have been detected. However, platinum is present because it has been deposited to protect the sample during FIB procedure and silicon and molybdenum can be found in the support of the lamella, namely the nano-mesh shown in figure 4.10. A low presence of chromium can also be detected. Maps shown in figure 6.22 represent the results obtained for the investigation on iron, nickel, oxygen and sulfur. Nickel and iron maps show respectively two darker and lighter lines which can be transalated in an excess and shortage of the corresponding element. When those maps are compared, in figure 6.24, it can be seen that the darker layers in the nickel map correspond to lighter layers on the iron map and viceversa. Considering the fact that the investigated sample is composed on average by half nickel and half iron, the hypothesis that can be made is that there is a local variation of the atomic ratio of Ni over Fe. About the distribution of other investigated elements, EELS analysis carried out in the same region (fig. 6.25 and 6.27) can provide further information. In particular, in figure 6.26, sulfur, carbon and oxygen are portrayed. The color scale indicates with red and yellow spots the regions in which the element is more present, while in blue the ones in which it has not been detected. Sulfur map does not provide any certain result because the colours do appear very sparse, hence it could be present in a very low amount which makes it not feasible for the instrument to be measured properly or it could be homogeneously disperse. Oxygen can be observed close to the top surface, it is very clear its distribution around the indenter tip mark. Carbon is expected to be found at columnar grain boundaries and the big red dot in the map, size around $30 - 50nm$ is coherent with such statement.

The focus of computer simulation of nanoindentation test, as shown in figure 6.28, is on the contact between sample and Berkovich indenter spherical tip. In figure 6.28, colour gradient standing for deformation has to be satisfied at first by few triangulation elements. It still carries a sufficient degree of accuracy if the general size of

the problem, micrometric scale, is considered compared to the size of the investigated interaction, nanometric scale. In fact, each element involved in the displacement representation is smaller than $1nm$. A discontinuity effect due to this choice of meshing can be seen also in figure 6.29. Finer meshes could be adopted to eliminate such effect, but it would require a far more performant processor. However, it is more interesting, at this point, to observe the interaction between the specimen and the indenter as the indentation depth increases. In figure 6.30, deformation is still due to the rounded tip of the indenter, while figure 6.31 shows the transition to planar indentation. It is here that creep phenomena might be investigated and analysed, at first. Results shown in previous pictures are coherent with experimental indentation depths encountered during real life tests and deformation contours are semi-spherical as expected from theoretical studies.

Conclusions

8

Interest in electrodeposited nanocrystalline Ni-Fe alloys is growing due to their mechanical, thermal and magnetic properties. In this work nanoindentation tests have been performed on both top surface and cross section surface. Tests performed on top surface showed a decrease of measured Young's modulus values for ascending peak loads, while tests performed on cross section surface recorded higher values of Young's modulus for experiments carried out in a region close to top surface, rather than nearby bottom surface. The influence of loading rate has been investigated on both annealed and as deposited samples.

A step segment has been pointed out in the loading portion of the load-displacement curves and it can represent a transition from grain boundary sliding deformation mechanism to deformation mechanism involving dislocations. The investigation of different loading rates lead to considerations on creep. It has been shown that for high loading rates, the time-displacement graph traced for hold time only, shows an exponential trend, while for lower loading rates a three segment linear beahaviour is a better fitting. In addition, for low loading rates creep of the tested material can be better investigated without the contribution of creep due to thermal effects.

SEM observation of regions on cross section surface of both annealed and as deposited sample showed a larger grain size close to top surface, while when comparing the two samples, it results that the specimen which did not undergo heat treatment has a bigger grain size, on average. With TEM observation some nanaograins have been measured and the region below indentation mark has been investigated with diffraction patterns and dark field images. Diffraction patters obtained in different points of the lamella are characteristic of an FCC structure.

EBDS performed with EDS highlighted columnar grain boundaries and the possibility to encounter impurities in said regions. EDS analysis, both with SEM and TEM, showed the disptribution of carbon, oxygen and sulfur. EELS with TEM showed a more clear distribution of oxygen on top surface and the presence of localized carbides.

The computer simulation of the nanoindentation test with Berkovich indenter has been implemented by adding, for meshing purposes only, a small cylinder and a tri-lobed geometry in the sample. The former has been designed to investigate the transition from spherical indentation, due to the round tip of the indenter, to planar indentation, while the latter has been designed in such a way to comply with the motion of the indenter. Both are keys to understand creep behaviour of the specimen. Besides, the introduction of these geometries made the partialization of a non axial symmetric model possible, saving on computation costs.

Aknowledgments

Thank you to Professor Giovanni Maizza for giving me the opportunity to join this research project and for passionately sharing his work to help me develop my curiosity and knowledge towards new topics. Thank you for giving me the instruments and support to make choices for my professional future.

Thank you to his group, Frediano De Marco, Umid Jamalov and Renato Pero, at "Centro di modellazione multifisica dei materiali e dei processi" at Politecnico di Torino, for sharing their ideas in an open and stimulating environment and actively supporting my work with COMSOL Multiphysics.

Thank you to Professor Takahito Ohmura for giving me the opportunity to perform experimental work at "National Institute for Materials Science" in Tsukuba and to work with many experts, from whom I could learn a lot. Thank you for your time, suggestions and for opening a new world of possibilities and knowledge to me.

Thank you to his group "High Strength Materials Group" at "Research Center for Structural Materials - NIMS". Thank you to Mrs. Misato Souissi and her family and Mrs. Rie Iguchi for their full support during my stay. Thank you to Dr. Eri Nakagawa for teaching and assisting me with samples preparation, nanoindentation tests and providing answers to all my questions. Thank you to Dr. Ya-Ling Chan for her time and incredible work with FIB samples preparation, TEM observation, analysis and explanation of each step. Thank you to Ta-te Chen, Dayuan Liu, Viola Paul and Zhengzhong Sun for sharing your time, ideas, dreams and tea breaks with me.

Thank you to Professor Toru Hara for giving me access to the "Stuctural Materials Analysis Platform" with "Microstructural Analysis Group", where I experienced incredibly valuable learning moments. Thank you to Dr. Yuka Hara for the work performed with SEM observation, EBSD and EDS and to Dr. Taku Moronaga for the work performed with TEM EDS and EELS. Thank you for sharing your comments, ideas and paving the way to further challenging research developments.

Finally, I am deeply grateful to you all for making me feel at home on the other side of the globe.

Grazie ai miei compagni di avventura Frank, Mattia e Piero. Il percorso non avrebbe avuto lo stesso significato se non lo avessi condiviso con voi.

Grazie a Danilo, Michela e Pietro perchè "si scrive Collegio e si legge famiglia" anche quando non si vive più sotto lo stesso tetto.

Grazie a Genni per farmi prendere la rincorsa nelle buone idee e tirare il freno a mano in quelle meno buone.

Grazie ad Arianna e Patti per esserci state in ogni momento, sempre pronte ad incoraggiarmi ed ascoltarmi.

Grazie ad Andrea, Francesco e Massimiliano perchè non importa dove saremo e quali strade la vita ci porterà a prendere, sarete sempre una mia certezza.

Grazie ai miei zii e cugini. La nostra famiglia ha sempre imparato a mancarsi, ma la gioia di avervi qui oggi è immensa.

Grazie a nonna per avere sempre una parola giusta per me e per essere sempre supersprint.

Grazie a HeyPolvia per aver raccolto tutti i miei pensieri e avermi dato la possibilità di archiviare ogni emozione in pochi tratti.

Grazie a mia sorella Alice, il presidente, per mostrarmi ogni giorno nuovi motivi per essere felice.

Grazie ai miei genitori che mi danno sempre la possibilità e il coraggio di credere in nuovi sogni e costruire le mie strade per realizzarli.

Bibliography

[1] Edax, *www.edax.com*.

[2] Eels educational website, *www.eels.com*.

[3] Electron diffraction patterns, *www.tcd.ie*.

[4] Gatan, *www.gatan.com*.

[5] Hysitron triboindenter, *www.bruker.com*.

[6] Jeol, *www.jeol.co.jp/en/*.

[7] Oxford instruments - ebsd, *www.ebsd.com*.

[8] Zeiss, *www.zeiss.com*.

[9] Hongbin Bei, Easo P George, JL Hay, and George Mathews Pharr. Influence of indenter tip geometry on elastic deformation during nanoindentation. *Physical review letters*, 95(4):045501, 2005.

[10] Vineet Bhakhri and Robert J Klassen. Haasen plot activation analysis of constant-force indentation creep in fcc systems. *MRS Online Proceedings Library Archive*, 1049, 2007.

[11] Esteban Broitman. Indentation hardness measurements at macro-, micro-, and nanoscale: a critical overview. *Tribology Letters*, 65(1):23, 2017.

[12] ZH Cao, L Wang, K Hu, YL Huang, and XK Meng. Microstructural evolution and its influence on creep and stress relaxation in nanocrystalline ni. *Acta Materialia*, 60(19):6742–6754, 2012.

[13] Yuanfeng Cheng and Li Xue. On dislocation absorption in grain boundaries. *DEStech Transactions on Engineering and Technology Research*, (apetc), 2017.

[14] et al. Cheung. electrodeposition of nanocrystalline ni-fe alloys.. *Nanostructured Materials*, vol. 5(no. 5):,pp. 513523, 1995.

[15] Didier Chicot, Patrick De Baets, MH Staia, ES Puchi-Cabrera, G Louis, Y Perez Delgado, and Jef Vleugels. Influence of tip defect and indenter shape on the mechanical properties determination by indentation of a tib2–60% b4c ceramic composite. *International Journal of Refractory Metals and Hard Materials*, 38:102–110, 2013.

[16] Didier Chicot, M Yetna NJock, Francine Roudet, Xavier Decoopman, MH Staia, and ES Puchi-Cabrera. Some improvements for determining the hardness of homogeneous materials from the work-of-indentation. *International Journal of Mechanical Sciences*, 105:279–290, 2016.

[17] In-Chul Choi, Byung-Gil Yoo, Yong-Jae Kim, and Jae-il Jang. Indentation creep revisited. *Journal of Materials Research*, 27(1):3–11, 2012.

[18] AH Chokshi, A Rosen, J Karch, and H Gleiter. On the validity of the hall-petch relationship in nanocrystalline materials. *Scripta Metallurgica*, 23(10):1679–1683, 1989.

[19] T Chudoba and F Richter. Investigation of creep behaviour under load during indentation experiments and its influence on hardness and modulus results. *Surface and Coatings Technology*, 148(2-3):191–198, 2001.

[20] K Durst, O Franke, A Böhner, and M Göken. Indentation size effect in ni–fe solid solutions. *Acta materialia*, 55(20):6825–6833, 2007.

[21] F Ebrahimi, D Kong, TE Matthews, Q Zhai, TS Srivastan, and KA Khor. Processing and fabrication of advanced materials vii, 1998.

[22] F Ebrahimi and HQ Li. Structure and properties of electrodeposited nanocrystalline fcc ni-fe alloys. *Reviews on Advanced Materials Science*, 5(2):134–138, 2003.

[23] AA Elmustafa, S Kose, and DS Stone. The strain-rate sensitivity of the hardness in indentation creep. *Journal of materials research*, 22(4):926–936, 2007.

[24] T Elridge. Achieving industry integration with nanomaterials through financial markets. *Nanotechnology Now*, 2014.

[25] G Feng and AHW Ngan. Effects of creep and thermal drift on modulus measurement using depth-sensing indentation. *Journal of materials research*, 17(3):660–668, 2002.

[26] Richard P Feynman. There's plenty of room at the bottom. *California Institute of Technology, Engineering and Science magazine*, 1960.

[27] GE Fougere, L Riester, M Ferber, JR Weertman, and RW Siegel. Young's modulus of nanocrystalline fe measured by nanoindentation. *Materials Science and Engineering: A*, 204(1-2):1–6, 1995.

[28] H Gleiter. Nanostructured materials: basic concepts and microstructure. *Acta materialia*, 48(1):1–29, 2000.

[29] Kenta Goto, Ikumu Watanabe, and Takahito Ohmura. Determining suitable parameters for inverse estimation of plastic properties based on indentation marks. *International Journal of Plasticity*, 116:81–90, 2019.

[30] Ferdinand Hofer, Franz-Philipp Schmidt, Werner Grogger, and Gerald Kothleitner. Fundamentals of electron energy-loss spectroscopy. In *IOP Conference Series: Materials Science and Engineering*, volume 109, page 012007. IOP Publishing, 2016.

[31] Tamás Kolonits, Péter Jenei, Bence G Tóth, Zsolt Czigány, Jenő Gubicza, László Péter, and Imre Bakonyi. Characterization of defect structure in electrodeposited nanocrystalline ni films. *Journal of The Electrochemical Society*, 163(3):D107–D114, 2016.

[32] Vlastimil Králík and Jiří Němeček. Comparison of nanoindentation techniques for local mechanical quantification of aluminium alloy. *Materials Science and Engineering: A*, 618:118–128, 2014.

[33] Minsu Lee, Jinho Ahn, and Tai Hong Yim. Effects of electroformed fe-ni substrate textures on light-trapping in thin film solar cells. *International Journal of Electrochemical Science*, 13(6):5612–5619, 2018.

[34] Hongqi Li and Fereshteh Ebrahimi. Tensile behavior of a nanocrystalline ni–fe alloy. *Acta Materialia*, 54(10):2877–2886, 2006.

[35] Hongqi Li, Fereshteh Ebrahimi, Hahn Choo, and Peter K Liaw. Grain size dependence of tensile behavior in nanocrystalline ni–fe alloys. *Journal of materials science*, 41(22):7636–7642, 2006.

[36] HQ Li and F Ebrahimi. An investigation of thermal stability and microhardness of electrodeposited nanocrystalline nickel-21% iron alloys. *Acta Materialia*, 51(13):3905–3913, 2003.

[37] G Maizza, H Eom, M Lee, TH Yim, E Nakagawa, R Pero, and T Ohmura. Mechanical and fracture behaviour of the three-scale hierarchy structure in as-deposited and annealed nanocrystalline electrodeposited ni–fe alloys. *Journal of Materials Science*, 54(20):13378–13393, 2019.

[38] Isao Matsui, Tomo Kawakatsu, Yorinobu Takigawa, Tokuteru Uesugi, and Kenji Higashi. Fabrication of bulk nanocrystalline fe–ni alloys with high strength and high ductility by an electrodeposition. *Materials Letters*, 116:71–74, 2014.

[39] Isao Matsui, Hiroki Mori, Tomo Kawakatsu, Yorinobu Takigawa, Tokuteru Uesugi, and Kenji Higashi. Mechanical behavior of electrodeposited bulk nanocrystalline fe-ni alloys. *Materials Research*, 18:95–100, 2015.

[40] E Mazza, S Abel, and J Dual. Experimental determination of mechanical properties of ni and ni-fe microbars. *Microsystem Technologies*, 2(4):197–202, 1996.

[41] Jonathan L McCREA, G Palumbo, GD Hibbard, and U Erb. Properties and applications for electrodeposited nanocrystalline fe-ni alloys. *Reviews on Advanced Materials Science*, 5(3):252–258, 2003.

[42] Jaroslav Menčík. Uncertainties and errors in nanoindentation. *Nanoindentation in Materials Science*, 54:53–86, 2012.

[43] N Moharrami and SJ Bull. A comparison of nanoindentation pile-up in bulk materials and thin films. *Thin Solid Films*, 572:189–199, 2014.

[44] TO Mulhearn and D Tabor. Creep and hardness of metals: a physical study. *J. Inst. Met*, 89(1):7–12, 1960.

[45] Tomio Nagayama, Takayo Yamamoto, and Toshihiro Nakamura. Thermal expansions and mechanical properties of electrodeposited fe–ni alloys in the invar composition range. *Electrochimica Acta*, 205:178–187, 2016.

[46] TG Nieh and J Wadsworth. Hall-petch relation in nanocrystalline solids. *Scripta Metallurgica et Materialia*, 25(4):955–958, 1991.

[47] CS Pande, RA Masumura, and RW Armstrong. Nanostruct. mater, 1993.

[48] Nurot Panich, Virasak Kraivichien, and Sun Yong. Finite element simulation of nanoindentation of bulk materials. *Journal of Scientific Research of Chulalongkorn University*, 29(2):145–153, 2004.

[49] María Teresa Pérez-Prado, Gaspar González-Doncel, Oscar Antonio Ruano, and TR McNelley. Texture analysis of the transition from slip to grain boundary sliding in a discontinuously recrystallized superplastic aluminum alloy. *Acta materialia*, 49(12):2259–2268, 2001.

[50] GM Pharr and WC Oliver. Measurement of thin film mechanical properties using nanoindentation. *Mrs Bulletin*, 17(7):28–33, 1992.

[51] Mehedi Reza, Eero Kontturi, Anna-Stiina Jääskeläinen, Tapani Vuorinen, and Janne Ruokolainen. Transmission electron microscopy for wood and fiber analysis- a review. *BioResources*, 10(3):6230–6261, 2015.

[52] Timothy J Rupert, Jonathan C Trenkle, and Christopher A Schuh. Enhanced solid solution effects on the strength of nanocrystalline alloys. *Acta Materialia*, 59(4):1619–1631, 2011.

[53] Z Shi, X Feng, Yonggang Huang, J Xiao, and KC Hwang. The equivalent axisymmetric model for berkovich indenters in power-law hardening materials. *International Journal of Plasticity*, 26(1):141–148, 2010.

[54] Richard W Siegel and Gretchen E Fougere. Mechanical properties of nanophase metals. *Nanostructured Materials*, 6(1-4):205–216, 1995.

[55] Dejan Stojakovic. Electron backscatter diffraction in materials characterization. *Processing and application of ceramics*, 6(1):1–13, 2012.

[56] Seiichi Suzuki. Features of transmission ebsd and its application. *Jom*, 65(9):1254–1263, 2013.

[57] Ibro Tabakovic, Steve Riemer, Vladyslav Vasko, Victor Sapozhnikov, and Mark Kief. Effect of magnetic field on electrode reactions and properties of electrodeposited nife films. *Journal of The Electrochemical Society*, 150(9):C635–C640, 2003.

[58] A Takita, K Sasaki, K Ohguchi, and R Takeda. An effective area considering the principal stress to evaluate creep strain measured by indentation test. *Experimental Mechanics*, 55(6):1081–1091, 2015.

[59] Norio Taniguchi, Chuichi ARAKAWA, and Toshio KOBAYASHI. On the basic concept of'nano-technology'. In *Proceedings of the International Conference on Production Engineering, 1974-8*, volume 2, pages 18–23. , 1974.

[60] V Torabinejad, M Aliofkhazraei, S Assareh, MH Allahyarzadeh, and A Sabour Rouhaghdam. Electrodeposition of ni-fe alloys, composites, and nano coatings–a review. *Journal of Alloys and Compounds*, 691:841–859, 2017.

[61] Stuart Wright and Matt Nowell. Ebsd image quality mapping. *Microscopy and microanalysis : the official journal of Microscopy Society of America, Microbeam Analysis Society, Microscopical Society of Canada*, 12:72–84, 03 2006.

[62] T Yanai, T Akiyoshi, T Yamaguchi, K Takashima, T Morimura, M Nakano, and H Fukunaga. Effect of primary amines on magnetic properties of fe-ni films electroplated in a des-based plating bath. *AIP Advances*, 8(5):056106, 2018.

[63] WJ Zong, D Wu, and CL He. Radius and angle determination of diamond berkovich indenter. *Measurement*, 104:243–252, 2017.